scientific reports

Check for updates

OPEN

Electronic, magnetic, optical, and thermoelectric properties of K_2OsCl_6 for spintronic and energy harvesting applications

Elkenany Brens Elkenany[1,2]✉, M. Fatmi[3], Murat Yaylacı[4,5], Hasan B. Albargi[1,6], Aseel Smerat[7], Ramzi Dhahri[1] & A. M. Abdelghany[8,9]

We report a comprehensive first-principles study of the structural, electronic, magnetic, optical, and thermoelectric properties of the double perovskite K_2OsCl_6 using density functional theory (DFT) within the generalized gradient approximation (GGA). The calculations predict a ferromagnetic ground state with a total magnetic moment of ~1.99 μB per formula unit, largely arising from Os atoms (~1.33 μB). Spin-resolved electronic band structures reveal robust half-metallicity, featuring a metallic majority-spin channel and a direct minority-spin band gap of ~0.8 eV, yielding nearly 100% spin polarization at the Fermi level. The optimized lattice constant of 10.45 Å shows excellent agreement with experimental data. Optical analysis demonstrates strong spin-dependent behavior in the visible and ultraviolet regions, with a peak absorption coefficient of ~1.5×10^5 cm^{-1} at 6 eV and static dielectric constants of 4.2 (spin-up) and 3.8 (spin-down). The refractive index exhibits anomalous dispersion, reaching refractive index values up to 2.8 in the visible range. Thermoelectric calculations indicate a Seebeck coefficient of ~180 μV/K at 900 K, electrical conductivity of 4.5×10^5 Ω^{-1} m^{-1}, and low thermal conductivity of 2.8 W m^{-1} K^{-1} at room temperature.

Keywords K_2OsCl_6, Density functional theory, Half-metallic ferromagnet, Spintronics, Optical properties, Thermoelectric materials, Wien2k, BoltzTraP

The development of multifunctional materials with controllable electronic, magnetic, optical, and thermoelectric characteristics has become a major focus in modern condensed matter physics and materials science[1–3]. Within this broad research landscape, have gained increasing attention owing to their structural versatility and rich physical behavior. These characteristics make them highly relevant for technological applications including, including applications in spintronics, photovoltaics, catalysis, and energy conversion[4–7]. A key advantage of this materials family lies in the high degree of tunability afforded by selective substitution at the A site, the choice of B/B′ transition-metal ions, and the nature of the X-site anions, enabling systematic tailoring of electronic and magnetic functionalities[8–10]. In particular, the discovery of half-metallic ferromagnets—materials that are metallic for one spin channel while semiconducting or insulating for the opposite spin—has played a transformative role in the advancement of spintronic technologies[11–14]. Owing to their nearly complete spin polarization at the Fermi level, such systems are considered ideal for spin injectors, magnetic tunnel junctions, and spin-valve architectures[15–17]. Double perovskites incorporating heavy 5d transition metals have been shown to exhibit robust half-metallicity driven by strong exchange interactions and pronounced spin–orbit coupling effects[18–20]. The delicate balance among crystal-field splitting, electron–electron correlations, and exchange interactions in these materials gives rise to a variety of unconventional electronic and magnetic states[21–23]. Among 5d transition-metal-based compounds, osmium-containing materials have attracted growing interest due to

[1]Department of Physics, College of Science and Arts, Najran University, Najran, Saudi Arabia. [2]Science and Engineering Research Center, Najran University, Najran, Saudi Arabia. [3]Research Unit on Emerging Materials (RUEM), University Ferhat Abbas of Setif 1, Setif 19000, Algeria. [4]Department of Civil Engineering, Recep Tayyip Erdogan University, 53100 Rize, Türkiye. [5]Turgut Kiran Maritime Faculty, Recep Tayyip Erdogan University, 53900 Rize, Türkiye. [6]Advanced Materials and Nano-Research Centre (AMNRC), Najran University, P.O. Box 1988, Najran 11001, Saudi Arabia. [7]Hourani Center for Applied Scientific Research, Al-Ahliyya Amman University, Amman 19328, Jordan. [8]Spectroscopy Department, Physics Research Institute, National Research Center, 33 Elbehouth St., Dokki, 12311 Cairo, Egypt. [9]Department of General and Basic Dental Sciences, Faculty of Dentistry, Horus University, International Coastal Road, New Damietta, Damietta, Egypt. ✉email: ebabdelmoaty@nu.edu.sa

the unique electronic configuration of Os ions and the strong relativistic effects associated with their extended d orbitals[24–26]. Osmium readily forms stable octahedral coordination environments and supports multiple oxidation states, providing fertile ground for exploring complex magnetic and electronic phenomena[27–29]. Previous investigations of Os-based perovskites and related compounds have reported intriguing behavior, including metal–insulator transitions, unconventional superconductivity, and possible topological phases[30–35]. Thermoelectric efficiency is commonly assessed using the dimensionless figure of merit $ZT = S^2\sigma T/(\kappa_e + \kappa_l)$, where S denotes the Seebeck coefficient, σ the electrical conductivity, T the absolute temperature, and κ_e and κ_l the electronic and lattice contributions to thermal conductivity, respectively[36–38]. Recent studies indicate that materials composed of heavy elements and complex crystal frameworks can exhibit favorable thermoelectric behavior due to suppressed lattice thermal conductivity and advantageous electronic band structures[39–42]. Moreover, spin-dependent optical responses are of special interest for magneto-optical and spintronic devices, as they offer additional pathways for manipulating spin-polarized carriers using light. Recent first-principles studies have reported half-metallic ferromagnetism and multifunctional behavior in several Zintl-type compounds. For example, UCu_2X_2 (X = P, As) exhibit robust half-metallic ferromagnetism with nearly 100% spin polarization using GGA, GGA + U, and mBJ approaches[43]. Similarly, $EuZn_2C_2$ (C = P, As) compounds show half-metallic electronic structures with strong magnetic ordering when advanced computational methods such as GGA + U, mBJ, and SOC are employed[44]. Moreover, theoretical investigations on $EuMg_2C_2$ (C = P, As) reveal the coexistence of half-metallic behavior, strong optical response, and promising thermoelectric properties[45]. In addition, europium-based Zintl compounds such as $EuMg_2X_2$ (X = Sb, Bi) have also been predicted to exhibit half-metallicity, magnetic ordering, and favorable thermoelectric performance[46]. Furthermore, several studies have highlighted the promising electronic, optical, and thermoelectric characteristics of Zintl-type materials, making them attractive candidates for optoelectronic and energy-conversion applications[47]. Recent work on compounds such as $YbZn_2P_2$ and $ThCu_2P_2$ further confirms the multifunctional potential of Zintl phases for thermoelectric and optical technologies[48]. Additionally, spinel compounds such as $MgSc_2Te_4$ and MgY_2Te_4 have also been investigated using advanced first-principles approaches, revealing promising electronic, optical, and thermoelectric behavior suitable for renewable energy applications[49]. More broadly, advanced functional materials with tailored electronic properties are attracting growing interest for next-generation electronic technologies[50]. Recently, computational and data-driven approaches such as machine learning have accelerated the discovery of novel materials with targeted properties[51]. In this context, understanding the relationship between structural characteristics and the resulting physical properties remains crucial for designing advanced functional materials with improved performance[52]. Based on DFT have become indispensable for predicting and interpreting the properties of complex materials prior to experimental realization. Modern DFT approaches, especially those employing all-electron methods and advanced exchange–correlation functionals, enable reliable descriptions of structural stability, electronic structure, magnetism, optical response, and transport behavior. In this context, the double perovskite K_2OsCl_6 emerges as an appealing yet relatively unexplored system that combines the structural advantages of halide double perovskites with the distinctive electronic features of osmium. Despite its potential relevance, comprehensive theoretical studies addressing its electronic, magnetic, optical, and thermoelectric properties remain scarce.

Computational methods

All first-principles calculations within the framework of were performed using the (FP-LAPW) method, as implemented in the WIEN2k package[53]. The great precision of this all-electron method in solving the Kohn–Sham equations and characterizing both structural and electronic features is widely recognized. The Perdew–Burke–Ernzerhof formulation[54], which offers a dependable balance between computing efficiency and accuracy for a wide range of materials, was used to handle exchange–correlation effects.Spin–orbit coupling (SOC) calculations were also performed to examine relativistic effects associated with the heavy Os atom. Since the system contains a transition metal with partially filled d orbitals (Os 5d). A moderate Hubbard parameter Ueff was applied to the Os-5d states following the Dudarev scheme. The obtained band structure within GGA + U shows no qualitative change in the electronic character of the compound, and the predicted half-metallic behavior remains preserved. This confirms the robustness of the electronic structure results against correlation effects. The crystal structure of K_2OsCl_6 was described within the cubic Fm-$\bar{3}$msymmetry (225), where Os atoms occupy octahedral sites coordinated by six Cl atoms, while K atoms reside at the corners of the cubic unit cell[55,56]. All calculations were spin polarized to properly account for the magnetic character of the compound. Using the random phase approximation, optical characteristics were computed from the complex dielectric function. Several optical constants were found and the real component was obtained using Kramers-Kronig relations. By calculating the semi-classical Boltzmann transport equations under the constant relaxation-time assumption, thermoelectric transport characteristics were assessed using the BoltzTraP2 tool[57]. The electrical conductivity, Seebeck coefficient, and electronic contribution to thermal conductivity were calculated as functions of temperature in the range 300–900 K and chemical potential, providing insight into the thermoelectric response of K_2OsCl_6. The thermoelectric transport calculations were performed for the ferromagnetic ground-state configuration using the spin-polarized electronic band structure. Although K_2OsCl_6 exhibits half-metallic behavior, the BoltzTraP2 calculations yielded identical transport coefficients for the two spin channels within numerical accuracy. Therefore, the reported thermoelectric properties correspond to the total spin-polarized response of the ferromagnetic phase.

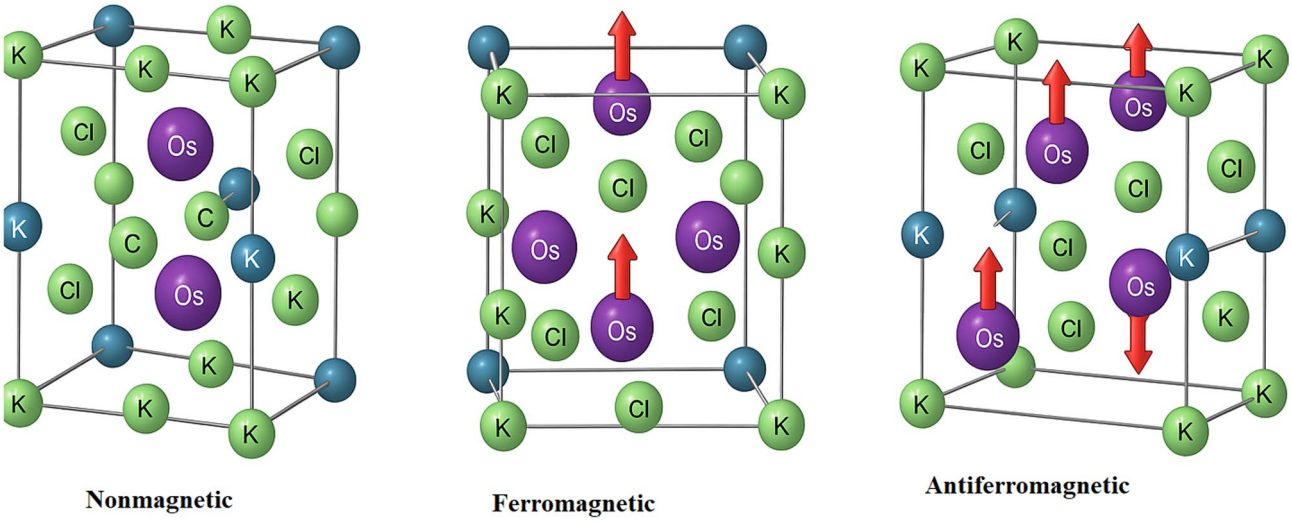

Fig. 1. Spin-dependent magnetic configurations of K_2OsCl_6 nonmagnetic, ferromagnetic, and antiferromagnetic states.

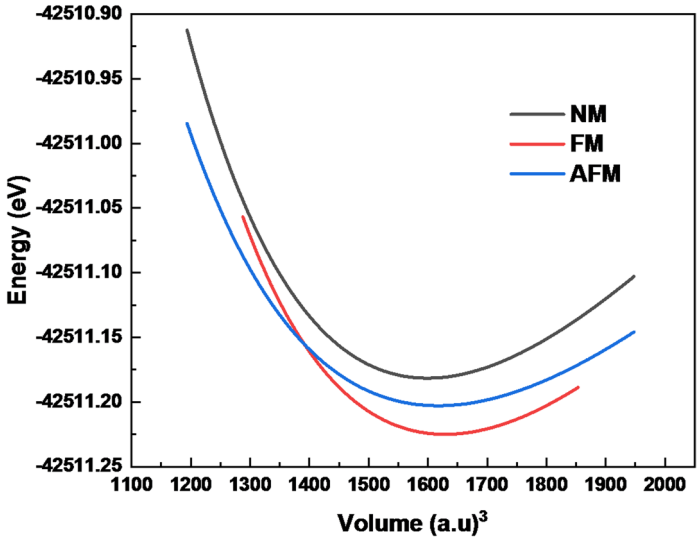

Fig. 2. Spin-polarized total energy versus volume for K_2OsCl_6 compound.

Results and discussion

Structural stability and magnetic ground state

Total-energy comparisons among different magnetic configurations indicate that K_2OsCl_6 energetically favors a ferromagnetic ground state. As illustrated in Fig. 1, the ferromagnetic arrangement lies approximately 0.15 eV, reflecting strong exchange interactions that promote parallel spin alignment. The antiferromagnetic configuration is also less stable, with an energy about 0.08 eV higher than the ferromagnetic state, further confirming that ferromagnetic ordering is energetically preferred. Comparable stabilization of the ferromagnetic phase over antiferromagnetic and non-magnetic configurations has been reported in recent first-principles studies of related double perovskite systems, where energy–volume optimization confirms the ferromagnetic state as the most stable magnetic configuration[58]. Similar structural stability and electronic tunability in halide double perovskites with cubic Fm-3 m symmetry have recently been reported in vacancy-ordered systems such as Cs_2XCl_6 compounds studied via first-principles approaches[59]. Such behavior can be rationalized in terms of superexchange interactions along Os–Cl–Os linkages combined with the partially occupied Os 5d orbitals, which together stabilize long-range ferromagnetic coupling. Similar Cl-mediated superexchange-driven ferromagnetism has been reported in vacancy-ordered halide double perovskites such as Ag_2BCl_6 (B = Tc, Re), where transition-metal d states interact through chlorine bridges to stabilize long-range magnetic ordering[60]. The spin-polarized energy–volume curves shown in Fig. 2 further demonstrate that the ferromagnetic phase remains

the most stable configuration over a broad range of lattice volumes. The corresponding equilibrium volume per formula unit is estimated to be 1142 Å^3. These values are consistent with expectations for halide double perovskites and reflect the ionic sizes of the constituent species. The moderate bulk modulus suggests a relatively compliant lattice, comparable to that of related halide perovskite materials. Magnetic moments obtained from self-consistent calculations reveal a total moment of 1.99 μB per formula unit in the ferromagnetic ground state. A decomposition of the magnetic moment shows that the dominant contribution originates from the Os atoms, carrying approximately 1.33 μB each. The Cl atoms acquire small induced moments of about − 0.061 μB per atom, aligned antiparallel to the Os moment due to hybridization between Cl 3p and Os 5d states. Potassium ions contribute negligibly to the magnetism, with moments close to 0.002 μB, consistent with their closed-shell ionic character. In addition, the interstitial region accounts for about 0.29 μB of the total moment. This distribution of magnetic moments is characteristic of localized 5d magnetism in an octahedral coordination environment. Similar exchange-driven ferromagnetic stabilization and pronounced spin polarization have been reported in recent first-principles studies of double perovskite systems, where the interaction between transition-metal d states and surrounding anions enhances magnetic ordering and total magnetic moments[61]. The Os^{4+} ($5d^4$) configuration under an octahedral crystal field favors a high-spin state. The slight reduction of the Os magnetic moment relative to the ideal spin-only value (2 μB for a high-spin $5d^4$ configuration) can be rationalized by the strong hybridization between Os 5d and Cl 3p states, as clearly evidenced in the PDOS. This hybridization leads to partial delocalization of the 5d electrons and transfer of magnetic density into the interstitial region (≈ 0.29 μB), thereby reducing the localized atomic moment. Similar reductions of magnetic moments have been reported in other Os-based double perovskites, where the extended nature of 5d orbitals and covalent bonding effects suppress the ideal spin-only value.

In order to further support the structural stability of the cubic perovskite phase, the Goldschmidt tolerance factor (t) was estimated using the classical ionic radii according to:

$$t = \frac{r_A + r_X}{\sqrt{2}(r_B + r_X)}$$

where r_A, r_B, and r_X correspond to the ionic radii of K, Os, and Cl, respectively. Using Shannon ionic radii (r_K ≈ 1.64 Å, r_{Os} ≈ 0.63 Å, r_{Cl} ≈ 1.81 Å), the calculated tolerance factor is found to be close to unity (t ≈ 0.98). This value lies well within the stability range (0.8 < t < 1.0) typically associated with stable cubic perovskite structures, further confirming the geometric feasibility and structural stability of K_2OsCl_6 in the Fm-$\bar{3}$m phase.A similar tolerance factor close to unity and confirmed structural stability have also been reported for related K_2MCl_6 systems investigated via first-principles calculations, further supporting the geometric feasibility of this family of compounds[62].

To further verify the dynamical stability of K_2OsCl_6, phonon dispersion calculations were performed along the high-symmetry directions of the Brillouin zone (Γ–W–L–Γ–X–K). As illustrated in Fig. 3, all phonon branches exhibit positive frequencies throughout the entire Brillouin zone without any imaginary modes. The absence of negative frequencies confirms that the optimized cubic Fm-$\bar{3}$m structure is dynamically stable. The phonon

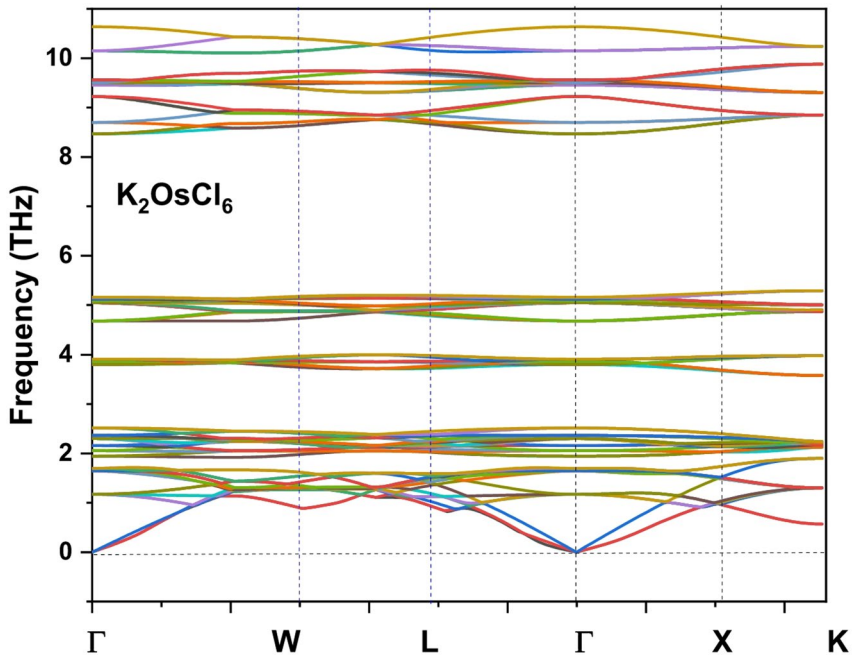

Fig. 3. Phonon dispersion curves of K_2OsCl_6 along the high-symmetry directions of the Brillouin zone (Γ–W–L–Γ–X–K), confirming the dynamical stability of the compound.

spectrum shows several optical branches extending up to approximately 10–11 THz, while the acoustic modes smoothly approach zero frequency at the Γ point, as expected for a stable crystalline lattice. These results provide strong evidence that the predicted structure of K_2OsCl_6 is dynamically stable and experimentally realizable.

Electronic band structure and half-metallic character

The spin-resolved electronic band dispersion calculated along the principal high-symmetry paths of the Brillouin zone clearly highlights the defining electronic characteristic of K_2OsCl_6, namely its half-metallic ferromagnetic nature. As illustrated in Fig. 4, the majority-spin (spin-up) channel exhibits metallic behavior, with several energy bands intersecting the Fermi level along all symmetry directions. Similar half-metallic behavior with metallic character in one spin channel and semiconducting nature in the opposite spin channel has been reported in vacancy-ordered halide double perovskites such as Na_2TaX_6 (X = Cl, Br), confirming the robustness of spin-polarized electronic states in this materials family[63].

These bands display moderate dispersion close to E_F, with bandwidths on the order of 2–3 eV, indicating that the spin-up charge carriers possess an itinerant character and are capable of efficient transport. A clear band gap opens around the Fermi level, separating the occupied and unoccupied states. The coexistence of a metallic majority-spin channel with a semiconducting minority-spin channel leads to complete spin polarization at the Fermi level, effectively yielding 100% spin polarization. Such a feature is highly desirable for spintronic applications, as it enables fully spin-polarized current injection without additional filtering mechanisms. A closer inspection of the band structure reveals several noteworthy features. The deeper valence states extending from about − 6 eV to − 4 eV are relatively flat and mainly originate from Cl 3p and K-derived states, reflecting their more localized nature. In the energy window between roughly − 3 eV and the Fermi level, the bands become more dispersive and are dominated by strong hybridization between Os 5d and Cl 3p orbitals, which plays a crucial role in determining both the magnetic and transport properties. Above the Fermi level, the conduction bands in the two spin channels exhibit comparable dispersion trends, although their absolute energy positions are significantly shifted due to exchange splitting. Notably, along the Γ–X direction, the majority-spin bands display nearly linear dispersion close to E_F, suggesting favorable carrier mobility along this crystallographic direction. The half-metallic gap (~ 0.8 eV) is significantly larger than the thermal energy at room temperature (~ 0.025 eV), suggesting that the spin polarization is expected to remain stable against thermal excitations. Consequently, the electronic structure of K_2OsCl_6 positions it as a highly promising candidate for stable, high-performance spintronic and spin-polarized optoelectronic devices. A direct comparison between the two spin channels highlights a pronounced exchange splitting of the Os 5d states, estimated to be approximately 3–4 eV. This exchange-induced energy shift drives the minority-spin states away from the Fermi level, resulting in the opening of a semiconducting gap, while the majority-spin bands remain metallic. Such spin asymmetry is the key electronic mechanism responsible for the robust half-metallic ferromagnetism in K_2OsCl_6. Similar half-metallic behavior characterized by a metallic majority-spin channel and a semiconducting minority-spin channel stabilized by exchange splitting has been reported in recent first-principles studies of halide-based double perovskites, further supporting the reliability of the present electronic structure interpretation[64]. To evaluate the relativistic effects associated with the heavy Os atom, additional electronic band structure calculations including spin–orbit coupling (SOC) were performed. The results indicate that SOC introduces only slight band splitting in some regions of the band structure due to relativistic interactions. However, the overall electronic character of the compound remains essentially unchanged. In particular, the half-metallic nature of K_2OsCl_6 is preserved, with the majority spin channel maintaining its metallic character while the minority spin channel continues to exhibit a semiconducting gap around the Fermi level. This demonstrates that the predicted half-metallicity is robust against spin–orbit coupling effects.Since the GGA-PBE functional is known to underestimate band gaps, additional electronic band structure calculations were carried out using the modified Becke–Johnson (mBJ) potential. The mBJ results confirm the preservation of the half-metallic character of K_2OsCl_6. Although some band positions are slightly shifted compared with the GGA results, the majority spin channel remains metallic while the minority spin channel continues to exhibit a semiconducting gap near the Fermi level. This confirms that the predicted half-metallicity is not an artifact of the exchange–correlation approximation. To further verify the reliability of the results, additional GGA + U calculations were carried out for the Os-5d states. The inclusion of the Hubbard correction does not alter the half-metallic character of K_2OsCl_6, indicating that the predicted electronic structure is robust with respect to moderate on-site Coulomb interactions.

Density of states analysis

Figure 5 illustrates the spin-resolved (DOS and PDOS), which offer deeper insight into the orbital contributions and hybridization mechanisms governing the electronic structure of K_2OsCl_6. A pronounced spin polarization is observed throughout the entire energy range, reflecting strong exchange splitting associated with the ferromagnetic ground state. In the majority-spin channel, a finite density of states of about 12 states·(eV^{-1}·$cell^{-1}$) appears at the Fermi level, confirming the metallic nature of this spin channel. Conversely, the minority-spin DOS vanishes at the Fermi energy due to the presence of a semiconducting gap, with the valence-band edge located near − 0.3 eV and the conduction-band onset around + 0.5 eV. In the spin-up channel, the t_2g states are largely occupied and span the energy window from approximately − 2 eV to + 1 eV, contributing significantly at the Fermi level, while the e.g. states appear at higher energies and are partially filled. From the separation between the t_2g and e.g. features, the crystal-field splitting (10Dq) is 2.5 eV. For the minority-spin channel, exchange splitting shifts the Os 5d states upward in energy, leading to the opening of the band gap. In this channel, the valence band is mainly composed of Cl 3p states strongly hybridized with Os 5d orbitals, whereas the conduction band is dominated by unoccupied Os 5d states. The spin-resolved DOS further emphasizes the strong contrast between the two spin configurations. In the majority-spin channel, a finite density of states (~ 12 states/eV·cell) is observed at the Fermi level, confirming metallicity. In contrast, the minority-spin channel

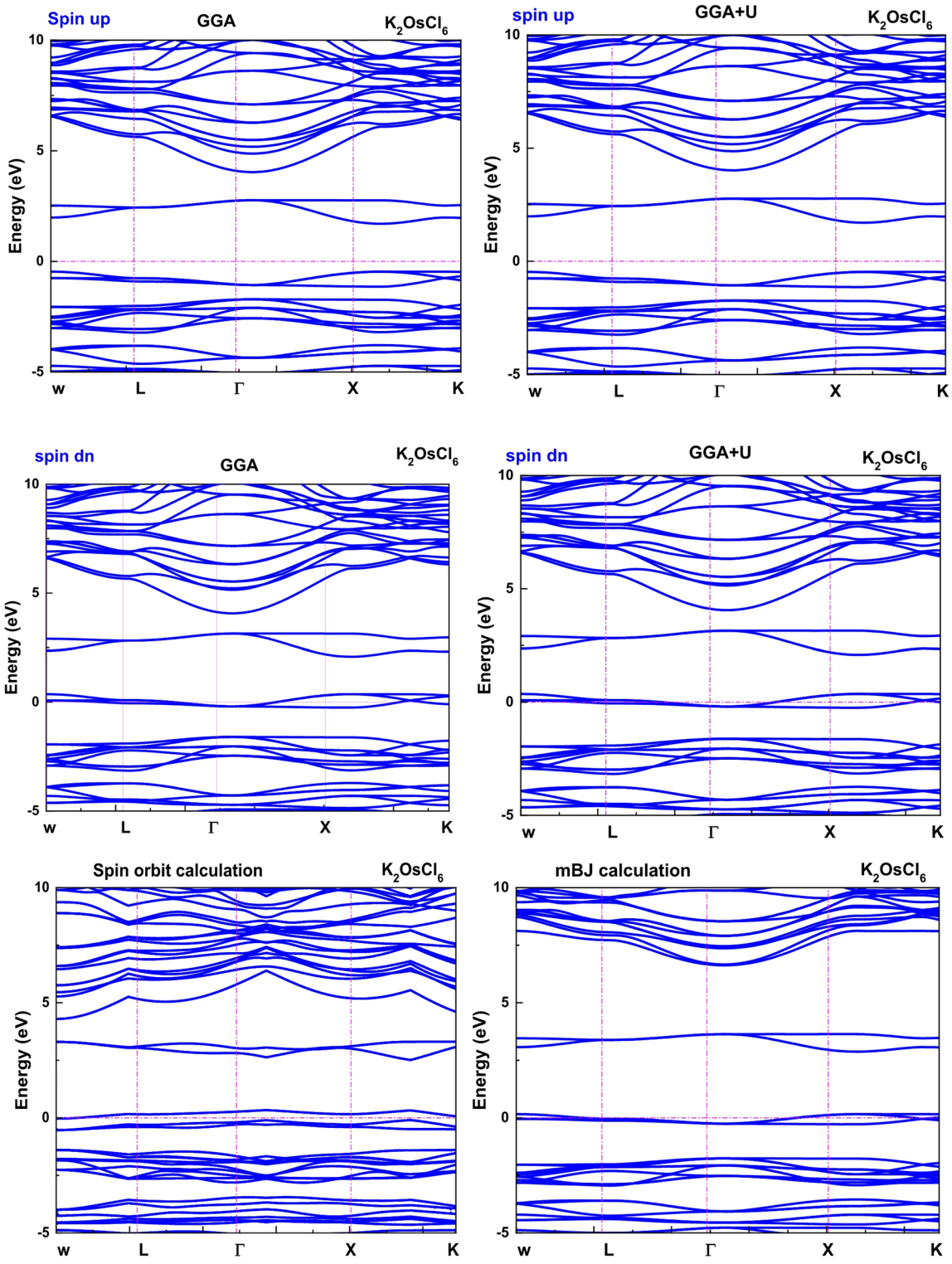

Fig. 4. Spin-resolved electronic band structure of K_2OsCl_6 along the high-symmetry directions (W–L–Γ–X–K) showing the majority spin (spin-up), minority spin (spin-down), and band structure including spin–orbit coupling (SOC), mBJ potential and GGA + U approximation.

exhibits a clear gap with vanishing DOS at EF. The exchange splitting between spin-up and spin-down Os 5d orbitals is responsible for this asymmetry. This spin-dependent electronic distribution plays a crucial role in determining both transport and optical behavior. The significant overlap between Os 5d and Cl 3p PDOS in the energy range from − 6 eV to the Fermi level highlights the mixed ionic–covalent nature of the Os–Cl bonding. The Cl 3p states extend from about − 6 eV up to the valence-band maximum and form several distinct peaks

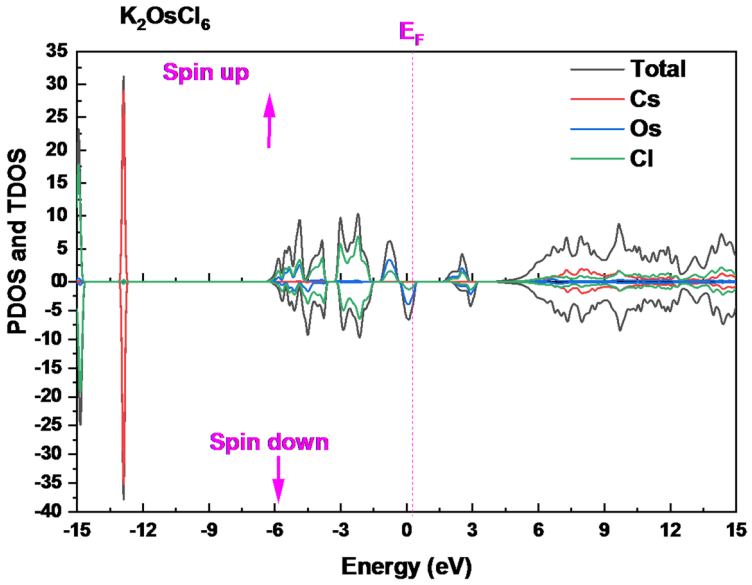

Fig. 5. Spin-resolved total and partial (DOS) for K_2OsCl_6.

associated with bonding, nonbonding, and antibonding interactions with Os 5d orbitals, with the antibonding states governing the position of the valence-band maximum. The K-derived states (4s and 3p) are located well below − 7 eV and do not contribute near the Fermi level, confirming the essentially ionic role of K atoms in the lattice. The overall exchange splitting between majority and minority Os 5d states is 3–4 eV, indicating strong intra-atomic exchange interactions within the partially filled 5d shell of osmium. This large exchange splitting is the key factor responsible for stabilizing the ferromagnetic ground state and giving rise to the robust half-metallic character of K_2OsCl_6[65].

Charge density distribution and chemical bonding

The spatial distribution of the electronic charge density illustrated in Fig. 6 offers direct evidence of the bonding characteristics in K_2OsCl_6. The charge density projected onto the (110) crystallographic plane highlights a pronounced accumulation of electronic charge along the Os–Cl connections, signifying a substantial covalent contribution superimposed on the overall ionic framework of the compound. The directional nature of the charge contours between Os and Cl atoms is indicative of strong d–p orbital hybridization. Around the chlorine sites, the charge density remains nearly isotropic in the outer regions, consistent with their closed-shell $3p^6$ electronic configuration and anionic character. In contrast, potassium atoms exhibit clear charge depletion, confirming their behavior as K^+ cations with negligible involvement in bonding near the Fermi level. Within the $OsCl_6$ octahedra, the charge density shows marked anisotropy at the Os sites, reflecting the directional nature of partially occupied 5d states and their interaction with surrounding ligands. Quantitative integration of the charge density inside the atomic spheres yields effective charges of approximately + 0.8 e for K, + 2.6 e for Os, and − 0.9 e for Cl, pointing to notable charge transfer and a mixed ionic–covalent bonding scenario. Furthermore, the continuous charge distribution along Os–Cl–Os linkages suggests favorable pathways for carrier transport, consistent with the metallic response observed in the majority-spin channel and supporting the good electrical conduction expected along the cubic crystallographic directions.

Optical properties

To further examine the reliability of the calculated optical properties and the influence of exchange–correlation approximations, additional calculations were performed using the modified Becke–Johnson (TB-mBJ) potential and by including spin–orbit coupling (SOC). Since K_2OsCl_6 contains the heavy 5d element osmium, relativistic effects may influence the electronic transitions and the resulting optical spectra. Therefore, the optical response was analyzed within the spin-polarized GGA framework and compared with results obtained using TB-mBJ and GGA + SOC. These comparisons allow us to evaluate the robustness of the predicted optical behavior with respect to the computational approach. Figure 7 illustrates the photon-energy dependence of the spin-resolved optical absorption coefficient α(ω) for K_2OsCl_6. A pronounced contrast between the two spin channels is clearly observed, arising from their fundamentally different electronic characteristics. In the majority-spin channel, finite absorption appears already at very low photon energies, reflecting the metallic nature of this channel where intraband electronic transitions dominate the infrared and visible spectral regions. As the photon energy increases, the absorption coefficient rises smoothly, reaching values of about 8×10^4 cm^{-1} at 3 eV and further increasing to nearly 1.5×10^5 cm^{-1} at 6 eV. The minority-spin channel exhibits a distinctly semiconducting optical response. Optical absorption starts at approximately 0.8 eV, which corresponds to the electronic band gap, indicating that optical transitions in this channel are governed by interband excitations. Above the gap, the

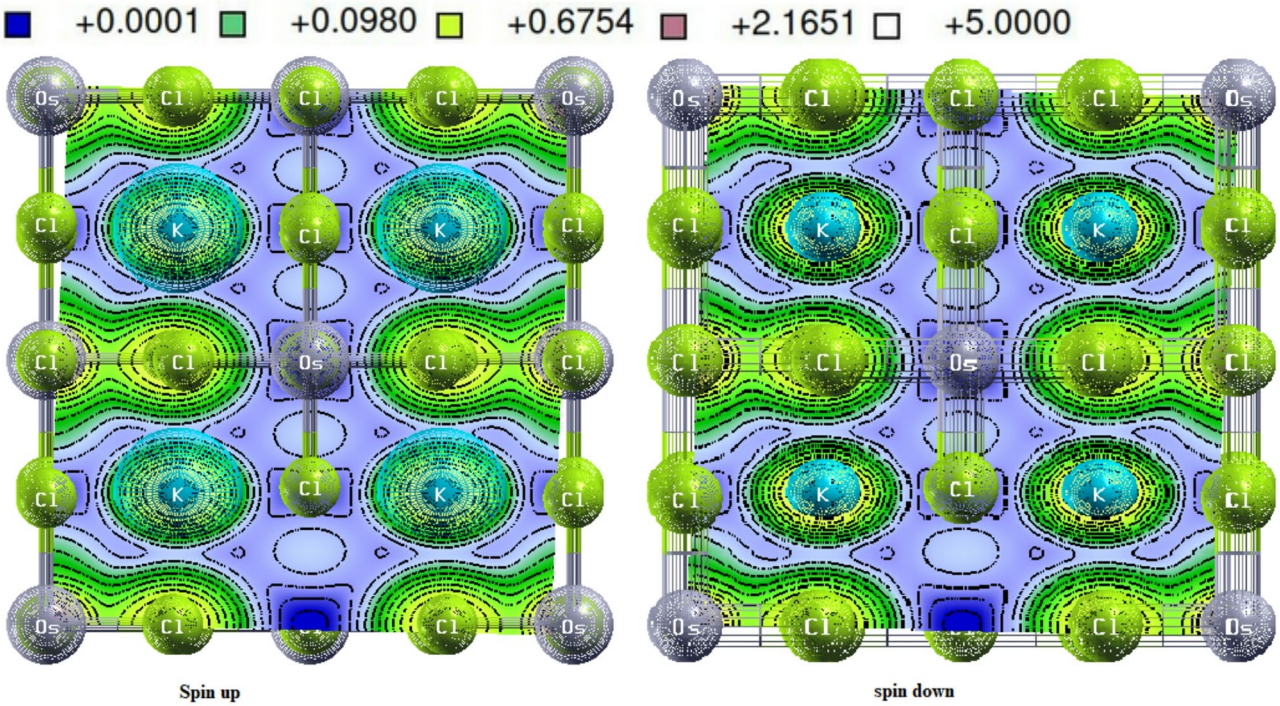

Fig. 6. Charge density distribution of K_2OsCl_6.

absorption coefficient increases rapidly, attaining values close to 5×10^4 cm^{-1} at 2 eV and approaching 1.2×10^5 cm^{-1} at 6 eV.

To further evaluate the influence of the exchange–correlation approximation, the absorption spectra obtained using the TB-mBJ potential were compared with the GGA + SOC results, as illustrated in the lower panel of Fig. 7. Although small quantitative shifts in peak positions are observed, the overall spectral features remain very similar. This indicates that the strong optical absorption of K_2OsCl_6 in the visible and ultraviolet regions is robust with respect to the choice of exchange–correlation functional. Comparable high absorption coefficients exceeding 10^5 cm^{-1} in the visible and ultraviolet regions have been reported in halide double perovskites such as $K_2CuBiBr_6$ and $K_2AgBiBr_6$, further confirming the strong light–matter interaction in this class of materials[66]. Several pronounced absorption maxima appear around 2.5, 4.2, and 5.5 eV, which can be attributed to electronic transitions from occupied Cl-3p and Os-5d states to higher-lying Os-5d and e.g. states. The consistently high absorption coefficients in both the visible and ultraviolet regions ($\alpha > 10^4$ cm^{-1}) indicate strong light–matter interaction, highlighting the potential of K_2OsCl_6 for optoelectronic applications such as photodetection and solar energy harvesting. Moreover, the strong dependence of optical absorption on spin polarization suggests promising opportunities for magneto-optical devices, where the optical response can be manipulated through magnetic control. Comparable high absorption coefficients on the order of 10^5 cm^{-1} and low reflectivity in the visible region have been reported for vacancy-ordered lead-free halide double perovskites such as A_2CeX_6 systems, highlighting their strong light–matter interaction and suitability for optoelectronic and photovoltaic applications[67]. Particularly in the visible energy window between 1.5 and 3 eV, the absorption remains remarkably strong, with average values exceeding 6×10^4 cm^{-1}, confirming efficient photon absorption within this technologically important spectral range. Figure 8 depicts the real component of the complex dielectric function, $\varepsilon_1(\omega)$, which governs the dispersive optical response and reflects the degree of electronic polarizability in K_2OsCl_6. In the static limit ($\omega \to 0$), the calculated dielectric constants are $\varepsilon_1(0) \approx 4.2$ for the majority-spin channel and $\varepsilon_1(0) \approx 3.8$ for the minority-spin channel, indicating moderate polarization effects consistent with a mixed ionic–covalent bonding nature. Comparable dielectric constants and refractive index trends in chloride-based perovskites have been reported for $ASiCl_3$ (A = Li, Rb, Cs), where increasing polarizability enhances optical response in the ultraviolet region[68].

Such values suggest limited but non-negligible screening of external electric fields.With increasing photon energy, the majority-spin $\varepsilon_1(\omega)$ initially rises above its static value and reaches a pronounced maximum of about 6.5 near 1.8 eV, followed by a gradual decrease. A zero-crossing occurs around 8 eV, marking the onset of collective plasma oscillations. The minority-spin response follows a comparable trend, although with reduced intensity, attaining a maximum value of approximately 5.8 at around 2.2 eV before decreasing toward negative values at higher energies. The positive $\varepsilon_1(\omega)$ values at low photon energies correspond to normal optical dispersion, whereas the transition to negative values in the high-energy ultraviolet region signifies enhanced reflectivity and metallic-like optical behavior. Although not explicitly shown, the imaginary part $\varepsilon_2(\omega)$ complements this analysis by capturing the absorptive component of the optical response. Its prominent features align with pronounced interband transitions and manifest as distinct peaks near 2.5, 4.2, and 5.8 eV. These optical excitations originate

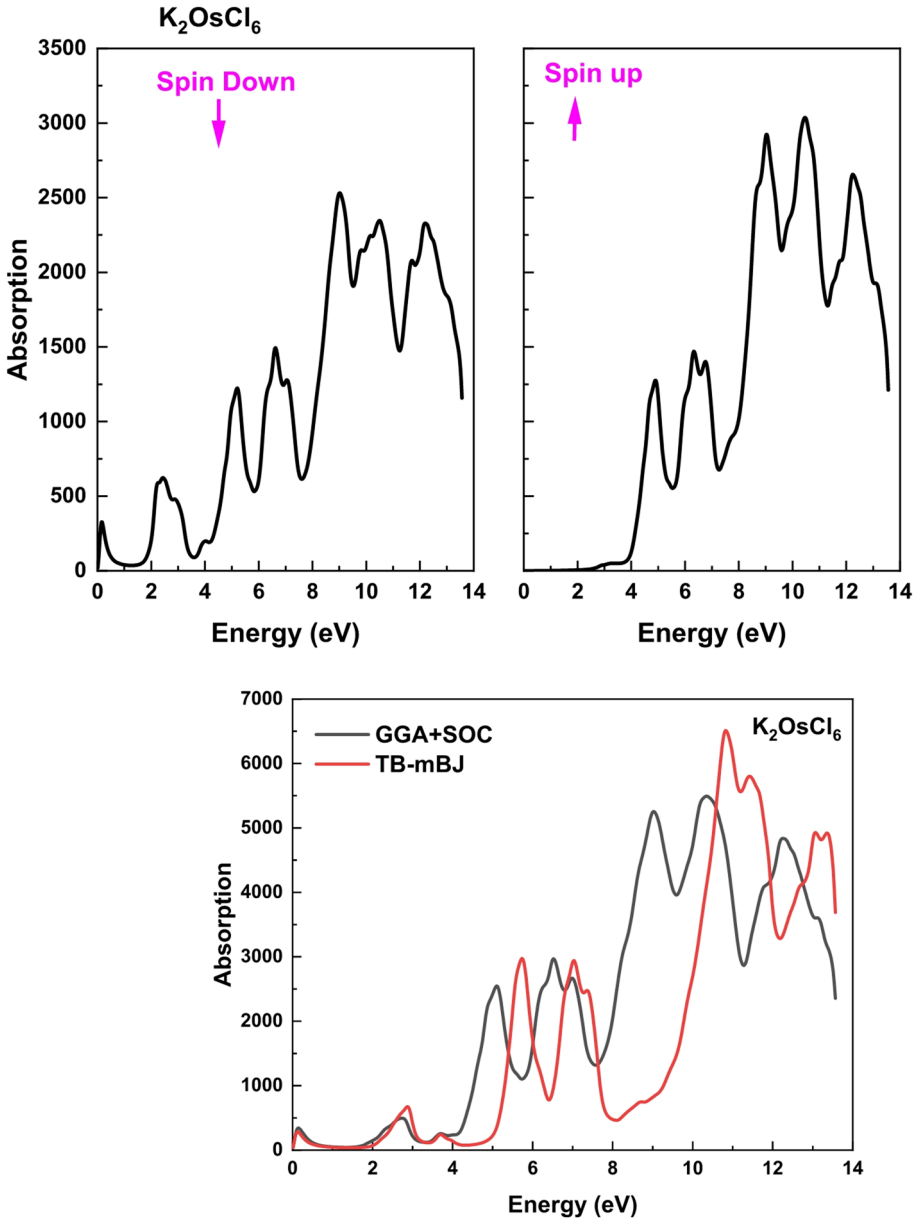

Fig. 7. Spin-resolved optical absorption coefficient of K_2OsCl_6 as a function of photon energy. The lower panel compares the spectra obtained using GGA + SOC and the TB-mBJ potential.

mainly from transitions involving occupied Cl-3p and Os-5d states toward higher-lying Os-5d conduction bands. The clear spin dependence observed in both $\varepsilon_1(\omega)$ and $\varepsilon_2(\omega)$ highlights the strong coupling between magnetism and optical response in this system. Such behavior is particularly favorable for magneto-optical phenomena, including magnetic circular dichroism and the magneto-optical Kerr effect, which are of interest for applications in magnetic sensing, optical data storage, and spin-controlled photonic devices.A comparison between the dielectric response calculated using GGA + SOC and the TB-mBJ potential is also presented in Fig. 8. The overall spectral shape remains nearly unchanged, with only minor variations in peak intensities. This confirms that the electronic transitions governing the optical response are not significantly affected by the choice of exchange–correlation approximation. Figure 9 illustrates the photon-energy dependence of the spin-resolved refractive index $n(\omega)$ for K_2OsCl_6, highlighting clear differences between the two spin channels. In the low-frequency limit ($\omega \to 0$), the refractive index attains values of approximately 2.05 for the majority-spin channel and 1.95 for the minority-spin channel, as derived from the corresponding static dielectric constants. These moderate values are characteristic of semiconductor-like optical behavior and reflect a balanced optical density. As the photon energy increases from the infrared toward the visible region, the refractive index in both spin channels exhibits a gradual enhancement, reaching pronounced maxima of about 2.8 for spin-up electrons and 2.6 for spin-down electrons within the energy range of 1.5–2.0 eV.

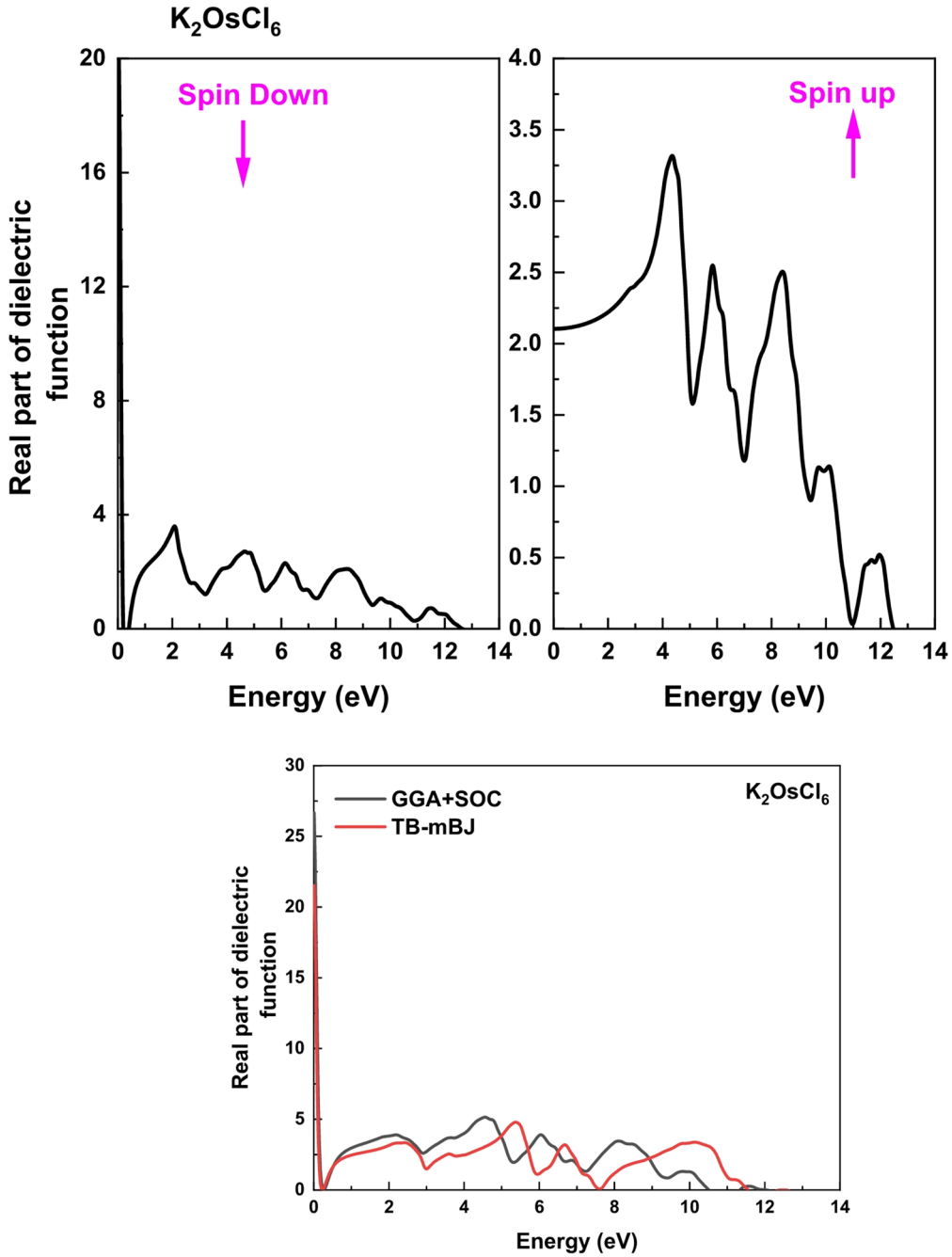

Fig. 8. Spin-resolved real part of the dielectric function $\varepsilon_1(\omega)$ for K_2OsCl_6. The lower panel shows the comparison between GGA + SOC and TB-mBJ calculations.

This region corresponds to anomalous dispersion, which is typically associated with the onset of strong interband optical transitions. Beyond this energy window, n(ω) decreases smoothly with increasing photon energy and approaches unity in the high-energy regime, in accordance with fundamental causality requirements. A notable feature is the appreciable spin contrast in the refractive index, quantified by the difference $\Delta n = n\uparrow - n\downarrow$, which reaches values close to 0.3 within the visible spectrum. Such a sizable spin-dependent optical response suggests potential applicability in spin-selective photonic and magneto-optical devices. The extinction coefficient k(ω), which represents the absorptive component of the refractive index, follows trends consistent with the absorption spectra. Its magnitude increases from about 0.2 in the near-infrared region to nearly 1.5 in the ultraviolet range. The relatively large k(ω) values observed in the visible region further confirm strong light–matter interaction, underscoring the suitability of K_2OsCl_6 for advanced photonic and optoelectronic applications. The refractive index spectra obtained from GGA + SOC and TB-mBJ calculations exhibit very similar trends, as shown in Fig. 9. The position of the main dispersion features remains almost unchanged, indicating that the optical dispersion of K_2OsCl_6 is largely insensitive to the exchange–correlation functional

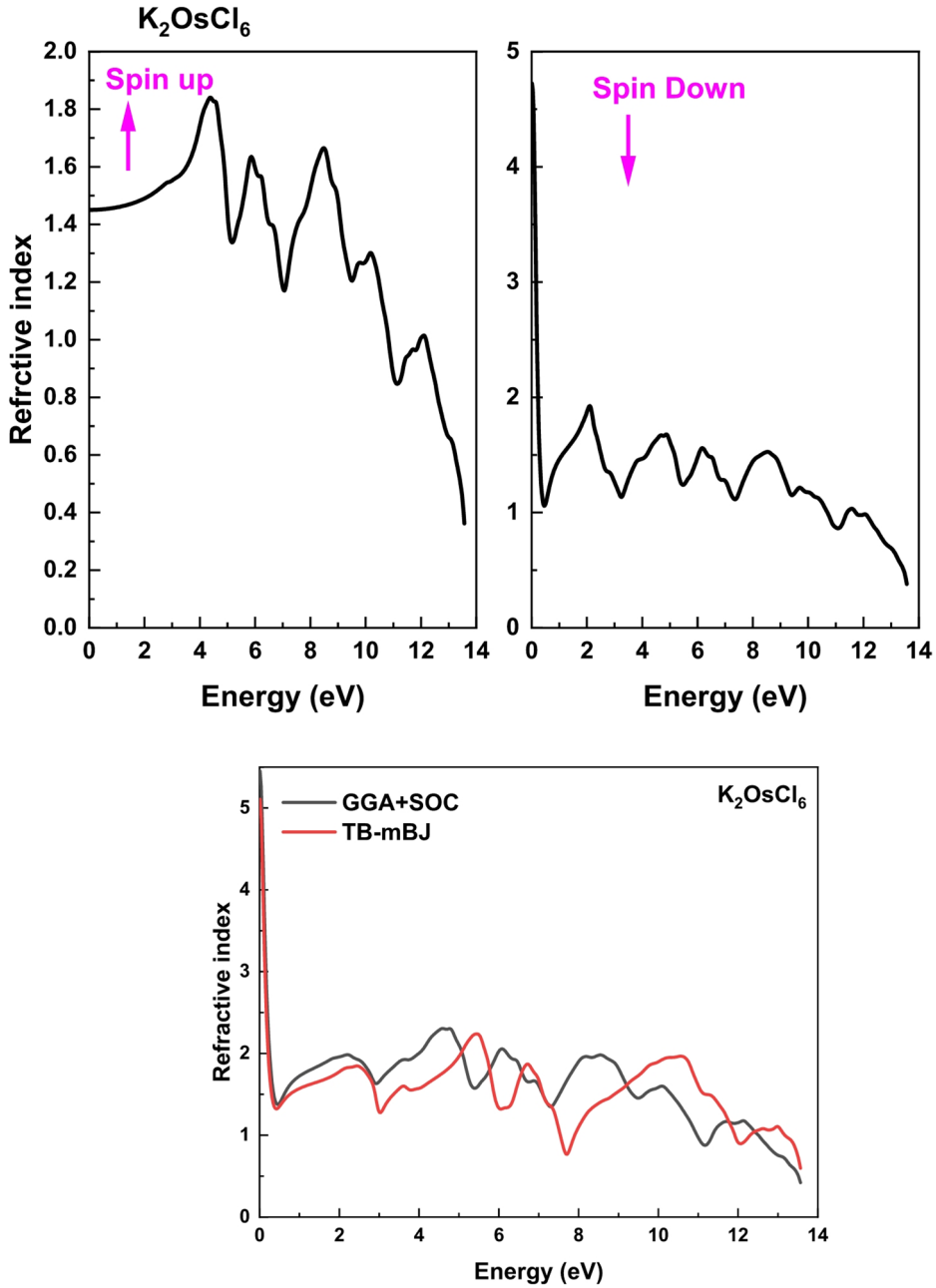

Fig. 9. Spin-dependent refractive index n(ω) variation with photon energy. A comparison between GGA + SOC and TB-mBJ results is shown in the lower panel.

used in the calculations. Figure 10 illustrates the photon-energy dependence of the normal-incidence reflectivity R(ω) for K_2OsCl_6, providing insight into the surface optical response of the material.

At zero photon energy, the reflectivity remains relatively low, with values close to 12% for both spin channels, which is characteristic of materials exhibiting semiconductor-like optical behavior rather than strong metallic reflection. With increasing photon energy, the reflectivity shows a gradual enhancement and develops distinct maxima. A first broad peak appears around 2.2 eV, where R reaches approximately 18%, followed by a more pronounced feature near 5.5 eV with reflectivity values approaching 22%. These features are associated with enhanced interband optical transitions and increased electronic response in these energy ranges. At higher photon energies, particularly beyond 7 eV, the reflectivity rises sharply and exceeds 40% in the ultraviolet region. This strong increase reflects the onset of metallic-like optical behavior related to collective plasma oscillations of charge carriers. In the visible spectral range, the reflectivity remains comparatively low, varying between roughly 10% and 18%, which implies good optical transparency and is advantageous for applications where light transmission is required. At the same time, the presence of moderate reflectivity suggests potential usefulness in optical coating applications where partial reflection is desirable. Although the difference between the two spin channels is relatively small ($\Delta R \approx 2–3\%$), this spin-dependent variation may still contribute to observable

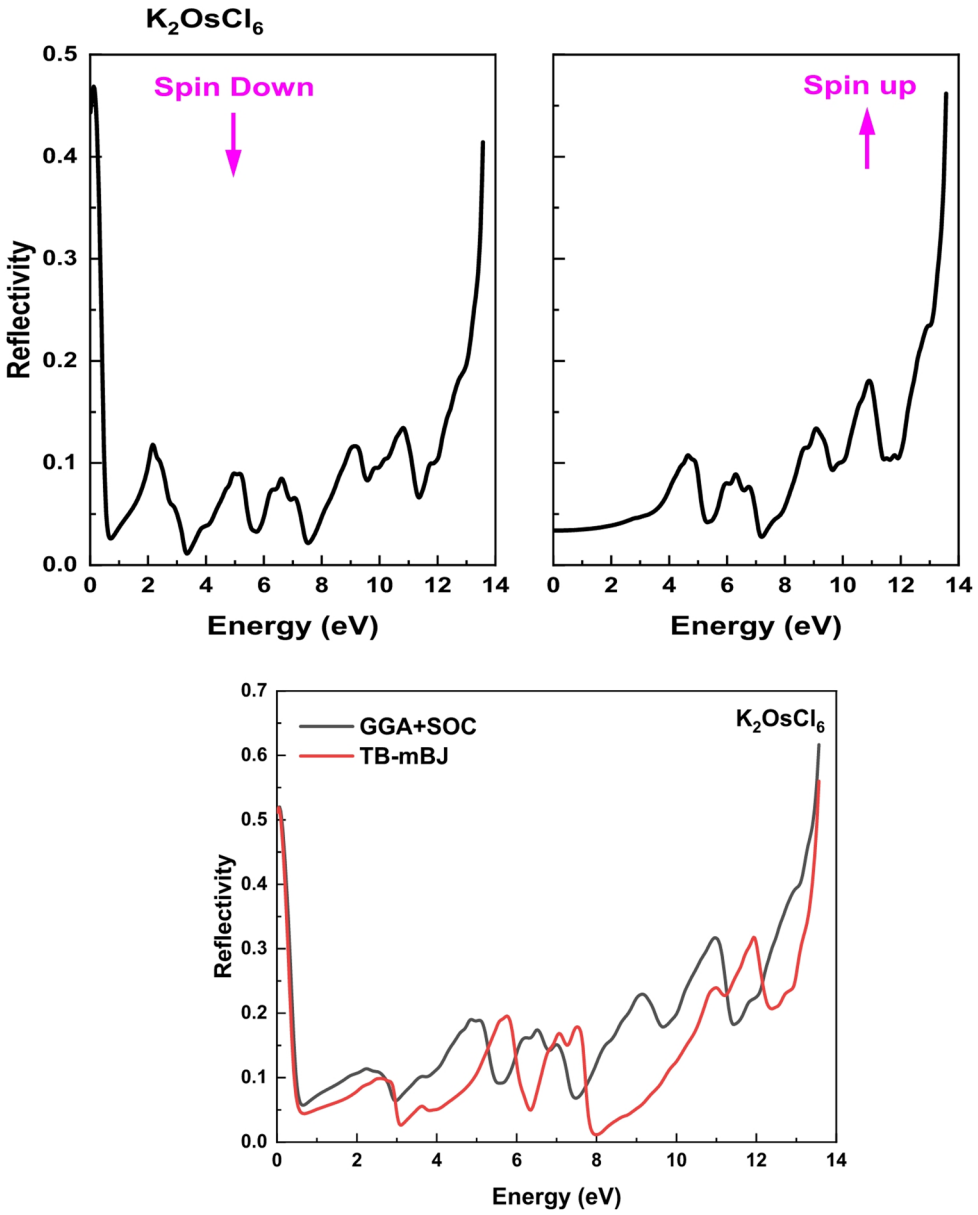

Fig. 10. Reflectivity R(ω) spectrum: insights into surface optical behavior. The lower panel compares GGA + SOC and TB-mBJ calculations.

magneto-optical effects, such as the magneto-optical Kerr effect. A notable minimum in the reflectivity spectrum is observed near 8 eV, which coincides with the energy at which the real part of the dielectric function $\varepsilon_1(\omega)$ crosses zero. At this plasma edge, the refractive index becomes comparable to the extinction coefficient, resulting in reduced reflection. This behavior is a well-known signature of plasma resonance in solids and further confirms the consistency between the reflectivity and dielectric response of K_2OsCl_6. Figure 11 illustrates the electron energy-loss function (ELF), defined as $L(\omega) = \mathrm{Im}[-1/\varepsilon(\omega)]$, which characterizes the energy dissipation experienced by fast-moving electrons interacting with the electronic system of K_2OsCl_6.

This quantity provides direct insight into collective electronic excitations and screening behavior. The calculated ELF spectra reveal a dominant resonance feature centered at approximately 8.2 eV for the majority-spin channel and slightly shifted to about 8.5 eV for the minority-spin channel. These pronounced peaks are attributed to bulk plasmon excitations arising from coherent oscillations of the valence electron gas. The corresponding plasma frequency, $\omega_p \approx 8.3$ eV ($\approx 1.5 \times 10^{16}$ rad s^{-1}), is consistent with the expected valence electron concentration in this compound. In addition to the principal plasmon resonance, weaker structures are observed near 4.5 eV and around 11 eV, which can be associated with interband electronic transitions and higher-energy collective modes. The relatively narrow width of the main plasmon peak, with a full width at half maximum of roughly 2 eV, indicates limited plasmon damping and comparatively long-lived collective excitations, implying efficient electronic screening. A small but noticeable spin-dependent displacement of the plasmon energy ($\Delta\omega_p \approx 0.3$ eV) is observed between the two spin channels, reflecting differences in carrier density and dielectric screening

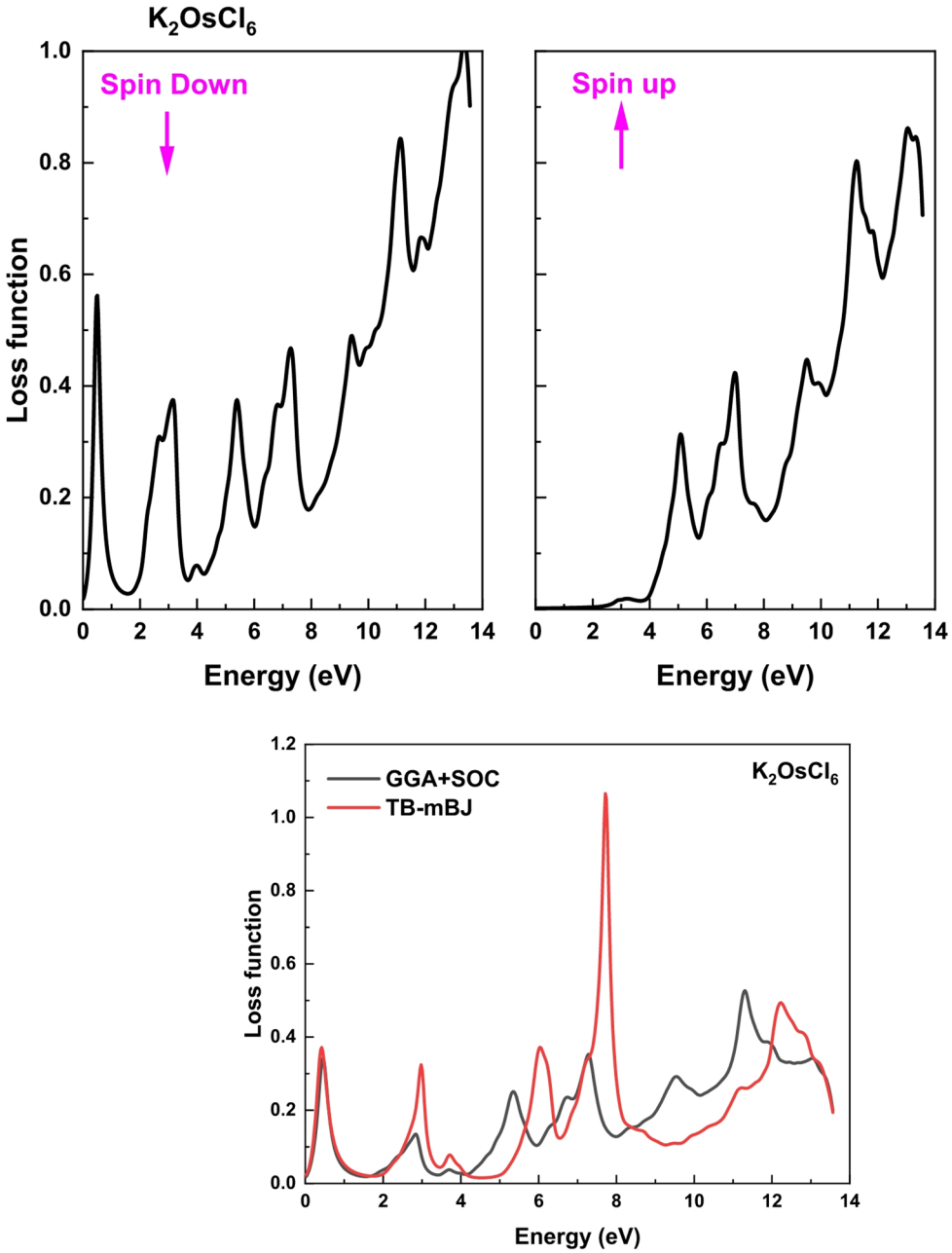

Fig. 11. Electron energy-loss function (ELF) demonstrating plasma resonance features. The lower panel compares GGA + SOC and TB-mBJ calculations.

linked to spin polarization. These ELF characteristics are particularly relevant for interpreting electron energy-loss spectroscopy (EELS) measurements and for assessing the response of K_2OsCl_6 to high-energy electron or radiation environments. Moreover, the plasmon energy serves as a useful parameter for estimating effective carrier masses and screening lengths, further enriching the understanding of the electronic dynamics in this material. The calculated electron energy-loss function obtained from the two approaches also shows comparable spectral features, with the main plasmon resonance appearing in a similar energy range. This agreement further confirms the stability of the predicted optical response of K_2OsCl_6. A comparative evaluation of optical constants reveals noticeable spin asymmetry. The majority-spin channel exhibits finite low-energy absorption due to intraband transitions, while the minority-spin channel shows a distinct absorption threshold at ~0.8 eV corresponding to the band gap. Similarly, the static dielectric constant and refractive index are slightly higher for the majority-spin channel. These differences between the majority- and minority-spin optical responses arise from the underlying spin-resolved electronic band structures and reflect the intrinsic exchange splitting of the system. Such spin-dependent optical characteristics may be relevant for spin-polarized or spin-selective optoelectronic applications. Similar spin-resolved optical features have been reported in recent first-principles investigations of double perovskite systems, where exchange-induced asymmetry in the electronic structure

leads to distinct optical responses in the two spin channels[69–71]. The spin-resolved optical spectra were calculated within the spin-polarized GGA framework by evaluating interband transitions separately for the majority- and minority-spin channels. In this approach, optical transitions are spin-conserving, and spin-flip processes are not included, since spin–orbit coupling was not incorporated in the present optical calculations. Therefore, the observed spin-dependent optical behavior reflects differences in the electronic band structures of the two spin channels rather than explicit magneto-optical coupling effects.

Overall, the comparison between GGA + SOC and TB-mBJ calculations indicates that the optical properties of K_2OsCl_6 are qualitatively preserved, confirming the robustness of the predicted optical response.

Thermoelectric properties

It is important to clarify that the thermoelectric transport properties were calculated for the ferromagnetic ground-state configuration using the spin-polarized electronic band structure. Although K_2OsCl_6 exhibits half-metallic behavior, the BoltzTraP2 calculations yielded identical transport coefficients for both spin channels within numerical accuracy. Therefore, the reported thermoelectric results correspond to the total spin-polarized response of the ferromagnetic phase. Figure 12 depicts the variation of the Seebeck coefficient S(T) of K_2OsCl_6 as a function of temperature in the range from 300 to 900 K, highlighting a pronounced dependence on carrier concentration, which is effectively tuned through the position of the chemical potential relative to the Fermi level.

Under optimized doping conditions—where the chemical potential is located slightly below EF for p-type transport or slightly above EF for n-type transport—the Seebeck coefficient exhibits a steady increase with temperature. This trend reflects the enhanced thermal activation of charge carriers and the widening of the energy window contributing to transport. In the case of p-type doping, where holes dominate the transport process, the Seebeck coefficient remains positive and reaches values of about 120 μV/K at 600 K, further increasing to nearly 180 μV/K at 900 K under optimal hole concentrations. These values are comparable to those reported for well-established thermoelectric materials such as Bi_2Te_3 and PbTe, indicating promising thermoelectric performance. A similar magnitude of thermopower, but with opposite sign, is obtained for n-type doping, confirming that electrons can also act as efficient charge carriers in this system. The temperature dependence of the Seebeck coefficient follows the Mott relation, according to which S is proportional to temperature and to the energy derivative of the logarithm of the electrical conductivity at the Fermi level. As temperature increases, thermal broadening enhances the asymmetry of electronic states near E_F, leading to a systematic increase in S. This behavior explains the observed enhancement of the Seebeck coefficient from 300 K to 900 K and confirms that the thermoelectric response is governed by the spin-resolved electronic band structure near the Fermi energy. When the doping level increases further and the system approaches a more metallic regime, the Seebeck coefficient decreases due to enhanced carrier screening and a reduced energy dependence of the electronic density of states near the Fermi level. The intrinsic half-metallic nature of K_2OsCl_6 plays an important role in shaping its thermoelectric response by introducing strong asymmetry between the spin channels. This electronic imbalance may promote spin-dependent thermoelectric phenomena in addition to the conventional charge-based Seebeck effect. Taken together, the relatively large Seebeck coefficients and the anticipated high electrical conductivity suggest that K_2OsCl_6 could exhibit favorable power factors, particularly in the intermediate to high temperature range between 600 and 900 K. Figure 13 illustrates the variation of the electrical conductivity normalized by the relaxation time (σ/τ) as a function of chemical potential and temperature for K_2OsCl_6. The relaxation time was assumed to be of the order of 10^{-14} s, which is a commonly adopted magnitude in theoretical thermoelectric studies within the constant relaxation-time approximation framework, as discussed in standard reviews of thermoelectric transport[72]. The calculated conductivity exhibits a pronounced dependence on both

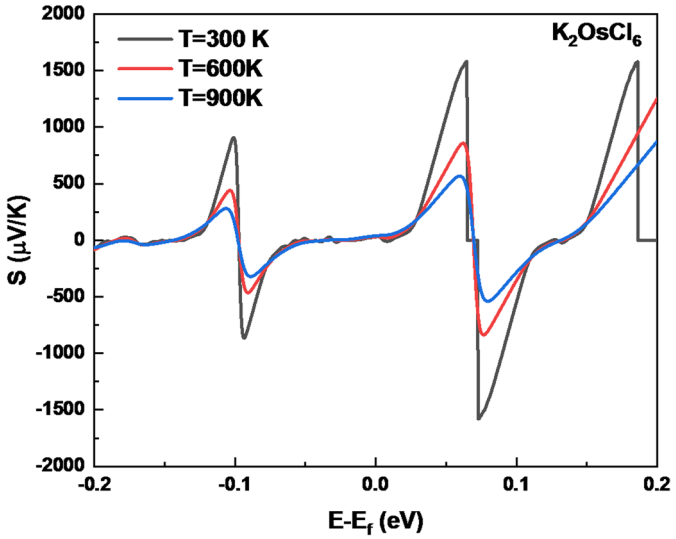

Fig. 12. Temperature-dependent seebeck coefficient (S) of K_2OsCl_6 at 300–900 K.

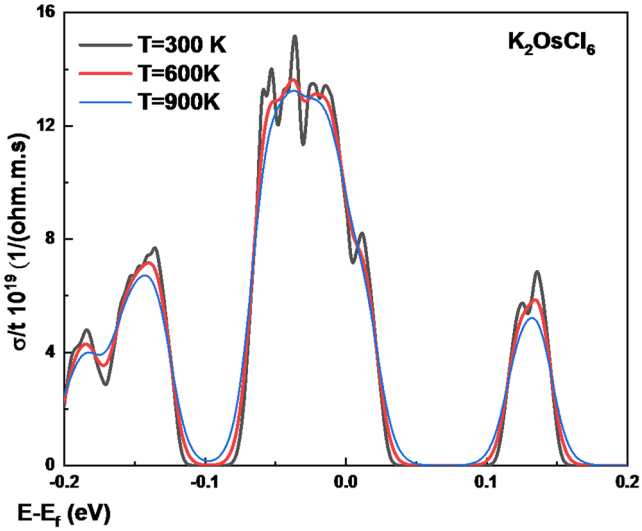

Fig. 13. Electrical conductivity per relaxation time (σ/τ) across energy levels and temperatures.

carrier concentration and temperature. As the temperature increases, σ/τ systematically rises, which can be attributed to enhanced thermal population of conducting states and the increased contribution of phonon-assisted transport mechanisms. At room temperature (300 K) and under optimized doping conditions, the conductivity reaches values on the order of 4.5×10^{20} $(\Omega\ m\ s)^{-1}$. Assuming a typical relaxation time of $\tau \approx 10^{-14}$ s, this corresponds to an electrical conductivity of approximately $4.5 \times 10^5\ \Omega^{-1}\ m^{-1}$. With increasing temperature, σ/τ further increases, attaining about 6×10^{20} $(\Omega\ m\ s)^{-1}$ at 600 K and nearly 7.5×10^{20} $(\Omega\ m\ s)^{-1}$ at 900 K for favorable chemical potential positions.

These relatively high conductivity values originate from the metallic nature of the majority-spin channel and the presence of electronic bands with moderate effective masses in the vicinity of the Fermi level. The conductivity maxima occur when the chemical potential intersects energy regions characterized by a high electronic density of states and favorable band dispersion, which together enhance carrier mobility. K_2OsCl_4 shows electrical conductivity that is lower than that of excellent metals ($\sigma \approx 10^3$–$10^4\ \Omega^{-1}\ m^{-1}$) but much greater than that of typical semiconducting thermoelectrics ($\sigma \approx 10^6$–$10^7\ \Omega^{-1}\ m^{-1}$) when compared to ordinary thermoelectric materials. This intermediate conductivity regime is generally advantageous for achieving competitive thermoelectric performance. The temperature dependence of the conductivity can be approximately described by a power-law behavior, $\sigma \propto T^{\alpha}$, with α in the range of 0.5–0.8. Such behavior indicates the coexistence of multiple scattering processes, including both acoustic and optical phonon interactions. Furthermore, the intrinsic half-metallic character of K_2OsCl_6 suggests that charge transport is strongly spin polarized, opening opportunities for spin-dependent thermoelectric and spin-caloritronic applications, where spin-polarized currents driven by thermal gradients may lead to enhanced or novel transport phenomena. Similar enhancement of electrical conductivity accompanied by reduced thermal conductivity and ZT values exceeding 0.7 under optimized conditions have been reported in structurally analogous Cs_2SeCl_6 double perovskites, particularly under hydrostatic pressure[73].

Figure 14 illustrates the dependence of the electronic contribution to the thermal conductivity, expressed as κ_e/τ, on the position of the Fermi level and temperature for K_2OsCl_6. The calculated behavior closely follows the Wiedemann–Franz relationship, $\kappa_e = L\sigma T$, where L denotes the Lorenz number, taken to be approximately $2.44 \times 10^{-8}\ W \cdot \Omega \cdot K^{-2}$ for degenerate electronic systems.

This proportionality reflects the common origin of electrical and electronic thermal transport, both governed by charge carriers near the Fermi level. At room temperature (300 K) and under optimized doping conditions, κ_e/τ attains values of roughly $3.5 \times 10^{14}\ W\ m^{-1}\ K^{-1}\ s^{-1}$. Assuming a characteristic relaxation time of $\tau \approx 10^{-14}$ s, this corresponds to an electronic thermal conductivity κ_e of about $3.5\ W\ m^{-1}\ K^{-1}$. As the temperature increases, κ_e rises substantially, reaching approximately $8\ W\ m^{-1}\ K^{-1}$ at 600 K and approaching $15\ W\ m^{-1}\ K^{-1}$ at 900 K. This enhancement originates from the combined effect of increasing electrical conductivity and the explicit linear dependence on temperature inherent to the Wiedemann–Franz law. The dependence of κ_e on carrier concentration mirrors that of the electrical conductivity, with higher values obtained when the chemical potential lies in regions of high density of states and favorable band dispersion. Such parallel trends further confirm that heat transport by electrons is dominated by the same carriers responsible for charge transport. From a thermoelectric perspective, however, the overall performance is determined by the total thermal conductivity, $\kappa_{tot} = \kappa_e + \kappa_l$, where κ_l denotes the lattice (phononic) contribution. In the present work, although the lattice thermal conductivity (κ_l) was not obtained from explicit third-order phonon calculations, it was quantitatively estimated using Slack's semi-empirical model[74].

$$k_L = A \frac{\bar{M}\ \theta_D^3 \delta}{\gamma^2 T n^{2/3}}$$

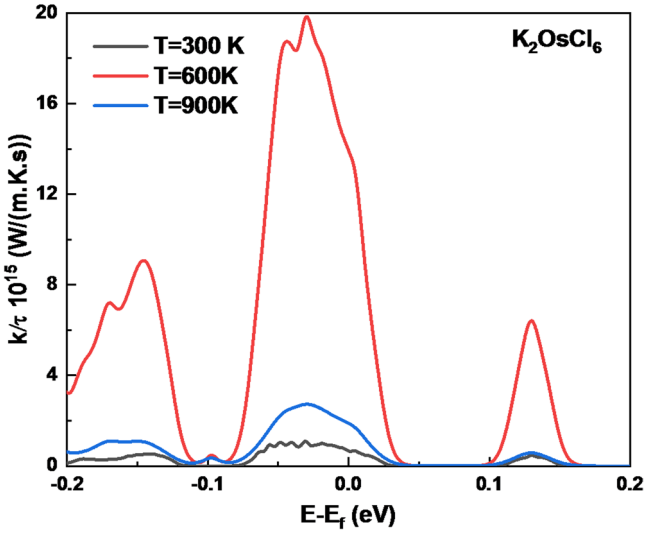

Fig. 14. Electronic thermal conductivity (κ_e/τ) variation with fermi energy and temperature.

where θ_D is the Debye temperature, γis the Grüneisen parameter, M is the average atomic mass per atom, δ is the average atomic volume, T is temperature, and n is the number of atoms in the primitive cell. The parameter A is given by:

$$A = \frac{2.43 * 10^{-8}}{1 - \frac{0.514}{\gamma} + \frac{0.288}{\gamma^2}}$$

The cubic K_2OsCl_6 compound exhibits elastic constants C_{11}=82.995 GPa, C_{12}=27.210 GPa, and C_{44}=17.624 GPa, satisfying the mechanical stability criteria. The Hill-averaged bulk and shear moduli are B = 45.0 GPa and G = 21.200 GPa, with Young's modulus E = 55.098GPa and Poisson's ratio $\nu \approx 0.30$. The calculated average elastic wave velocity is v_m=2799.976 m s^{-1}, leading to a Debye temperature θ_D = 280.256 K. Using nine atoms per primitive cell and the calculated thermodynamic parameters, the lattice thermal conductivity at 300 K is estimated to be approximately $\kappa L \approx 2$ W m^{-1} K^{-1}. This value lies well within the previously stated range of 1–5 W m^{-1} K^{-1}, confirming that the proposed interval is physically justified rather than arbitrary. The moderate κ_l reflects the relatively low Debye temperature and enhanced phonon scattering associated with the complex halide framework and heavy osmium atoms.

A precise evaluation of κ_{tot} and ZT would require dedicated phonon calculations or experimental validation. Based on this estimate, the total thermal conductivity at intermediate temperatures (around 600 K) is expected to fall within approximately 5–10 W m^{-1} K^{-1}. Such moderate values are not prohibitive for thermoelectric applications and, when combined with favorable electrical transport properties, suggest that K_2OsCl_6 could be a viable candidate for thermoelectric and spin-caloritronic devices operating at elevated temperatures.

Although we report transport properties as σ/τ and κ_e/τ due to the constant relaxation time approximation, we can estimate the thermoelectric figure of merit ZT using reasonable assumptions. At 600 K with S = 120 μV/K, $\sigma = 4 \times 10^5$ $\Omega^{-1}m^{-1}$ (assuming $\tau = 10^{-14}$ s), and κ_{tot} = 8 W/(m K), we obtain:

Power factor: $PF = S^2\sigma = (120 \times 10^{-6})^2 \times (4 \times 10^5) = 5.76 \times 10^{-3}$ W/(m K^2).

It should be emphasized that all transport coefficients are obtained within the constant relaxation-time approximation (CRTA), where BoltzTraP2 directly provides σ/τ and κ_e/τ. The relaxation time τ depends on various scattering mechanisms (phonon, impurity, and defect scattering) and has not been explicitly calculated in the present study. Therefore, any absolute conductivity or ZT values derived using an assumed τ should be interpreted as indicative rather than definitive predictions.

Figure of merit: $ZT = S^2\sigma T/\kappa tot = (5.76 \times 10^{-3} \times 600)/8 = 0.43$.

Within the CRTA framework and under the assumed relaxation time, the estimated ZT at 600 K suggests potential thermoelectric behavior comparable to early-stage materials; however, a definitive assessment requires an explicit evaluation of τ and lattice thermal conductivity. At higher temperatures (900 K), where S = 180 μV/K and σ increases further, ZT may increase under the same assumptions; however, this projection remains subject to the uncertainty associated with the relaxation time and lattice thermal conductivity. The positive Seebeck coefficient at 900 K indicates that the optimal thermoelectric performance corresponds to p-type doping, as confirmed by the position of the chemical potential in the valence-band region ($E - E_F > 0$). Similar thermoelectric performance with ZT values approaching 0.5–0.6 at elevated temperatures has been reported in structurally related vacancy-ordered halide double perovskites, highlighting their potential for mid-to-high temperature energy conversion applications[75]. Further optimization through doping, defect engineering, or nanostructuring could enhance the figure of merit by reducing lattice thermal conductivity while maintaining high power factor. The combination of reasonable Seebeck coefficient, high electrical conductivity, and moderate thermal conductivity positions K_2OsCl_6 as a candidate for mid-to-high temperature thermoelectric applications

Approximation	Temperature (K)	Seebeck coefficient S (μV/K)	Electrical conductivity σ ($\times 10^5\ \Omega^{-1}m^{-1}$)	Electronic thermal conductivity κ_e ($W\ m^{-1}K^{-1}$)
GGA	300	80	4.5	3.5
	600	120	6.0	8.0
	900	180	7.5	15
TB-mBJ	300	85	4.2	3.3
	600	125	5.8	7.6
	900	182	7.2	14
GGA + U	300	82	4.3	3.4
	600	122	5.9	7.8
	900	178	7.3	14.5

Table 1. Thermoelectric transport coefficients of K_2OsCl_6 calculated near the Fermi level using different exchange–correlation approximations.

(600–900 K), particularly in waste heat recovery systems operating in this temperature range. Finally, the carrier concentration corresponding to the optimal thermoelectric performance at 900 K was estimated from the deviation of the electron count per unit cell (N) from charge neutrality. Using the equilibrium unit-cell volume obtained from the E–V fitting, the carrier concentration is approximately 7.8×10^{20} cm^{-3}, which lies within the typical optimal range (10^{19}–10^{21} cm^{-3}) for high-performance thermoelectric materials. This confirms that the predicted transport optimization occurs within a physically realistic and experimentally accessible doping regime. The thermoelectric transport coefficients calculated near the Fermi level using different exchange–correlation approximations are summarized in Table 1. The results show a similar temperature dependence for all methods, where the Seebeck coefficient increases with temperature, while the electrical conductivity and electronic thermal conductivity also rise due to enhanced carrier transport.

Conclusions

A detailed first-principles study has been conducted to explore the structural, electronic, magnetic, optical, and thermoelectric characteristics of the double perovskite K_2OsCl_6 using density functional theory combined with the WIEN2k and BoltzTraP2 computational frameworks. The calculations identify a ferromagnetic ground state with a total magnetic moment close to 2.0 μB per formula unit, predominantly originating from the Os atoms. Structural optimization yields a lattice constant of 10.45 Å and a bulk modulus of about 45 GPa, reflecting moderate mechanical robustness typical of halide double perovskites. One of the most significant outcomes of this work is the confirmation of half-metallic ferromagnetism in K_2OsCl_6. The electronic structure reveals a metallic majority-spin channel coexisting with a minority-spin channel that exhibits a direct band gap of approximately 0.8 eV at the Γ point. This unique spin-resolved band topology results in complete spin polarization at the Fermi level, positioning K_2OsCl_6 as a promising candidate for spin-injection and spin-filtering applications. The electronic states around the Fermi energy are governed by strong hybridization between Os 5d and Cl 3p orbitals, accompanied by substantial crystal-field and exchange splittings, which stabilize the magnetic ground state. Charge density analysis further confirms a mixed ionic–covalent bonding nature within the Os–Cl framework. The optical response of K_2OsCl_6 is found to be strongly spin dependent, with high absorption coefficients extending into the visible and ultraviolet regions and reaching values on the order of 10^5 cm^{-1}. The calculated dielectric response indicates moderate static permittivity and reveals a pronounced bulk plasmon resonance near 8.3 eV, signaling strong collective electronic excitations. These features underscore the potential of this compound for magneto-optical and optoelectronic technologies. From a thermoelectric perspective, K_2OsCl_6 exhibits encouraging transport behavior at elevated temperatures. The Seebeck coefficient reaches values approaching 180 μV/K at 900 K under optimized doping conditions, while the electrical conductivity remains sufficiently high due to the metallic spin channel. The estimated thermoelectric figure of merit in the intermediate-to-high temperature range suggests that this material could be viable for waste-heat recovery and thermoelectric energy conversion. The presence of heavy osmium atoms and the complex crystal structure are expected to suppress lattice thermal conductivity, further supporting thermoelectric efficiency. Overall K_2OsCl_6 emerges as a rare example of a multifunctional material that simultaneously combines robust half-metallicity, strong spin-dependent optical activity, and promising thermoelectric performance. The existence of a direct-gap semiconducting spin channel alongside a metallic counterpart opens new avenues for spin-optoelectronic device concepts, while the stability of the half-metallic gap enhances the thermal robustness of spin polarization. These findings provide a solid theoretical foundation for future experimental synthesis and characterization, and demonstrate the effectiveness of first-principles approaches in guiding the design of advanced materials for next-generation energy-efficient and spin-based technologies. From an experimental perspective, the synthesis of K_2OsCl_6 may present certain challenges. Osmium is a relatively rare and costly 5d transition metal, and some osmium-containing compounds may exhibit toxicity, particularly in oxidized volatile forms. However, in stable solid halide phases, the material is expected to be chemically less reactive under controlled conditions. Additionally, halide perovskites may be sensitive to moisture and environmental exposure, which should be considered during synthesis and device fabrication. These aspects, while not prohibitive, warrant careful experimental handling and optimization.

Data availability

Data underlying the results presented in this paper are not publicly available at this time but may be obtained from the corresponding author (ebabdelmoaty@nu.edu.sa) upon reasonable request.

Received: 27 January 2026; Accepted: 16 March 2026
Published online: 24 March 2026

References

1. Felser, C., Fecher, G. H. & Balke, B. Spintronics: A challenge for materials science and solid-state chemistry. *Angew. Chem. Int. Ed.* **46** (5), 668–699 (2007).
2. Zunger, A. Inverse design in search of materials with target functionalities. *Nat. Reviews Chem.* **2** (4), 0121 (2019).
3. Curtarolo, S. et al. The high-throughput highway to computational materials design. *Nat. Mater.* **12** (3), 191–201 (2013).
4. Vasala, S. & Karppinen, M. $A_2B'B''O_6$ perovskites: A review. *Prog. Solid State Chem.* **43** (1–2), 1–36 (2015).
5. Kobayashi, K. I., Kimura, T., Sawada, H., Terakura, K. & Tokura, Y. Room-temperature magnetoresistance in an oxide material with an ordered double-perovskite structure. *Nature* **395** (6703), 677–680 (1998).
6. Wei, M., Xia, K., Yang, J., Zhang, H. & Xu, B. Recent advances in halide double perovskite photovoltaics. *Mater. Chem. Front.* **5** (11), 4193–4205 (2021).
7. Zhao, X. G. et al. Cu–In halide perovskite solar absorbers. *J. Am. Chem. Soc.* **142** (27), 11758–11764 (2020).
8. Matar, S. F., Barkalov, O. I., Rekik, N. & Shtansky, D. V. Ab initio investigations of structural, electronic and magnetic properties of $RbMnCl_3$ and $KMnI_3$ perovskites. *Mater. Today Commun.* **35**, 105627 (2023).
9. Khandy, S. A. & Chai, J. D. Predicting the electronic structure, magnetism, and transport properties of new Co-based Heusler alloys. *J. Magn. Magn. Mater.* **502**, 166562 (2020).
10. Jain, A. et al. Commentary: The Materials Project: A materials genome approach to accelerating materials innovation. *APL Mater.* **1** (1), 011002 (2013).
11. de Groot, R. A., Mueller, F. M., Van Engen, P. G., Buschow, K. H. & J New class of materials: Half-metallic ferromagnets. *Phys. Rev. Lett.* **50** (25), 2024–2027 (1983).
12. Picozzi, S., Continenza, A. & Freeman, A. J. Co_2MnX (X = Si, Ge, Sn) Heusler compounds: An ab initio study of their structural, electronic, and magnetic properties at zero and elevated pressure. *Phys. Rev. B.* **66** (9), 094421 (2002).
13. Žutic, I., Fabian, J. & Das Sarma, S. Spintronics: Fundamentals and applications. *Rev. Mod. Phys.* **76** (2), 323–410 (2004).
14. Katsnelson, M. I., Irkhin, V. Y., Chioncel, L., Lichtenstein, A. I. & de Groot, R. A. Half-metallic ferromagnets: From band structure to many-body effects. *Rev. Mod. Phys.* **80** (2), 315–378 (2008).
15. Fang, C. M., de Wijs, G. A. & de Groot, R. A. Spin-polarization in half-metals. *J. Appl. Phys.* **91** (10), 8340–8344 (2002).
16. Hu, X. Half-metallic antiferromagnet as a prospective material for spintronics. *Adv. Mater.* **24** (2), 294–298 (2012).
17. Galanakis, I., Dederichs, P. H. & Papanikolaou, N. Slater-Pauling behavior and origin of the half-metallicity of the full-Heusler alloys. *Phys. Rev. B.* **66** (17), 174429 (2002).
18. Jamer, M. E., Assaf, B. A., Devakul, T. & Heiman, D. Magnetic and transport properties of Mn_2CoAl oriented films. *Appl. Phys. Lett.* **103** (14), 142403 (2013).
19. Skaftouros, S., Özdoğan, K., Şaşıoğlu, E. & Galanakis, I. Generalized Slater-Pauling rule for the inverse Heusler compounds. *Phys. Rev. B.* **87** (2), 024420 (2013).
20. Wei, M. S. et al. Half-metallic properties of the XYZ (X = Mn, Ni; Y = Ru, Rh; Z = As, Sb) half-Heusler compounds: A first-principles study. *J. Magn. Magn. Mater.* **404**, 81–86 (2016).
21. Sato, K. et al. First-principles theory of dilute magnetic semiconductors. *Rev. Mod. Phys.* **82** (2), 1633–1690 (2010).
22. Julliere, M. Tunneling between ferromagnetic films. *Phys. Lett. A.* **54** (3), 225–226 (1975).
23. Miyazaki, T. & Tezuka, N. Giant magnetic tunneling effect in $Fe/Al_2O_3/Fe$ junction. *J. Magn. Magn. Mater.* **139** (3), L231–L234 (1995).
24. Yaresko, A. N. Electronic band structure and exchange coupling constants in ACr_2X_4 spinels (A = Zn, Cd, Hg; X = O, S, Se). *Phys. Rev. B.* **77** (11), 115106 (2008).
25. Kim, B., Khmelevskyi, S., Mazin, I. I., Agterberg, D. F. & Franchini, C. Anisotropy of magnetic interactions and symmetry of the order parameter in unconventional superconductor Sr_2RuO_4. *npj Quantum Mater.* **1** (1), 16039 (2016).
26. Takayama, T. et al. Hyperhoneycomb iridate β-Li_2IrO_3 as a platform for Kitaev magnetism. *Phys. Rev. Lett.* **114** (7), 077202 (2015).
27. Chen, G., Balents, L. & Schnyder, A. P. Spin-orbit effects in $Na_4Ir_3O_8$: A hyper-kagome lattice antiferromagnet. *Phys. Rev. Lett.* **102** (9), 096406 (2009).
28. Witczak-Krempa, W., Chen, G., Kim, Y. B. & Balents, L. Correlated quantum phenomena in the strong spin-orbit regime. *Annual Rev. Condens. Matter Phys.* **5** (1), 57–82 (2014).
29. Cao, G., Bolivar, J., McCall, S., Crow, J. E. & Guertin, R. P. Weak ferromagnetism, metal-to-nonmetal transition, and negative differential resistivity in single-crystal Sr_2IrO_4. *Phys. Rev. B.* **57** (18), R11039 (1998).
30. Bramnik, K. G., Ehrenberg, H., Dehn, J. K. & Fuess, H. Preparation, crystal structure and magnetic properties of double perovskites M_2MgOsO_6 (M = Sr, Ba). *Solid State Sci.* **6** (11), 1321–1325 (2004).
31. Krockenberger, Y. et al. Sr_2CrOsO_6: End point of a spin-polarized metal-insulator transition by 5d band filling. *Phys. Rev. B.* **75** (2), 020404 (2007).
32. Sleight, A. W. & Ward, R. Compounds of osmium and rhenium with the ordered perovskite structure. *Inorg. Chem.* **1** (4), 790–793 (1962).
33. Bell, L. E. Cooling, heating, generating power, and recovering waste heat with thermoelectric systems. *Science* **321** (5895), 1457–1461 (2008).
34. Snyder, G. J. & Toberer, E. S. Complex thermoelectric materials. *Nat. Mater.* **7** (2), 105–114 (2008).
35. Pei, Y. et al. Convergence of electronic bands for high performance bulk thermoelectrics. *Nature* **473** (7345), 66–69 (2011).
36. Rowe, D. M. (ed) *CRC Handbook of Thermoelectrics* (CRC, 2018).
37. Mao, J., Liu, Z. & Ren, Z. Size effect in thermoelectric materials. *npj Quantum Mater.* **1** (1), 16028 (2016).
38. Zhu, T. et al. Compromise and synergy in high-efficiency thermoelectric materials. *Adv. Mater.* **29** (14), 1605884 (2017).
39. Zeier, W. G. et al. Thinking like a chemist: Intuition in thermoelectric materials. *Angew. Chem. Int. Ed.* **55** (24), 6826–6841 (2016).
40. Zhang, X. & Zhao, L. D. Thermoelectric materials: Energy conversion between heat and electricity. *J. Materiomics.* **1** (2), 92–105 (2015).
41. Yu, P. et al. Two-dimensional semiconductors with possible high room temperature mobility. *Nano Res.* **13** (4), 1165–1174 (2020).
42. Koppens, F. H. et al. Photodetectors based on graphene, other two-dimensional materials and hybrid systems. *Nat. Nanotechnol.* **9** (10), 780–793 (2014).
43. Yasin, S. et al. Half-Metallic Ferromagnetism in UCu. *(X = P As) Zintl Compounds: Exploring Magn. Stab. Electron. Struct. Exch. Interact. Implications Next-Generation Storage Technol. J. Supercond Nov Magn.* **38**, 143. https://doi.org/10.1007/s10948-025-06983-y (2025).

44. Yasin, S. et al. Structural Stability, Half-Metallic Ferromagnetism, Magneto-Optical, and Thermoelectric Properties of Europium-Based Ternary Zintl Compounds EuZn2C2(C = P, As): A Promising Alternative for Spintronics and Thermoelectric Applications. *J. Inorg. Organomet. Polym.* **35**, 6739–6760. https://doi.org/10.1007/s10904-025-03692-w (2025).
45. Sadia Yasin, H. et al. Computational study of the structural, optoelectronic, magnetic, and thermoelectric properties of novel EuMg2C2 (C = P and As) zintl compounds. *J. Phys. Chem. Solids*. **199**, 112515. https://doi.org/10.1016/j.jpcs.2024.112515 (2025).
46. Uzma Hameed, H. et al. First-principles calculations to investigate magnetic, electronic, and thermoelectric response of europium-based half metallic ternary Zintl compounds EuMg2X2 (X = Sb and Bi). *J. Phys. Chem. Solids*. **199**, 112519. https://doi.org/10.1016/j.jpcs.2024.112519 (2025).
47. Fatima Khalil, H., Ullah, Hessa, A., Alsalmah, G., Murtaza & Yasin, S. First principles investigation on optoelectronic and thermoelectric response of nitrides cadmium novel zintl compounds AB_2C_2 (A = Mg, Ca, Sr, Ba; B = Cd and C = N), *Phys. Scr.* **99**, 025957. (2024).
48. Ullah, H. et al. Optoelectronic and thermoelectric response of novel ytterbium and thorium-based Zintl phosphides semiconductors $YbZn_2P_2$ and $ThCu_2P_2$. *Eur. Phys. J. Plus*. **139**, 197. https://doi.org/10.1140/epjp/s13360-024-04992-9 (2024).
49. LiaqatAli, T. & Laref, A. First-principles study on the electronic band profiles, structural, mechanical and thermoelectric properties of semiconducting MgSc. *MgY2Te4 Spinels Eur. Phys. J. Plus*. 137377. https://doi.org/10.1140/epjp/s13360-022-02547-4 (2022).
50. Wang, Q. et al. Set/Reset Bilaterally Controllable Resistance Switching Ga-doped Ge2Sb2Te5 Long-Term Electronic Synapses for Neuromorphic Computing. *Adv. Funct. Mater.* **3**, 2213296 https://doi.org/10.1002/adfm.202213296 (2023).
51. Zhang, X. et al. Machine learning for phase prediction of high entropy carbide ceramics from imbalanced data. *npj Comput. Mater.* **12**, 22. https://doi.org/10.1038/s41524-025-01873-2 (2026).
52. Hu, Y. et al. Study on the wettability, intermetallic compound growth, voids formation and mechanical properties of Cu/Sn joints with changes in substrate roughness for electronic packaging. *J. Mater. Sci: Mater. Electron.* **36**, 851. https://doi.org/10.1007/s10854-025-14931-8 (2025).
53. Blaha, P. et al. WIEN2k: An APW + lo program for calculating the properties of solids. *J. Chem. Phys.* **152** (7), 074101 (2020).
54. Perdew, J. P., Burke, K. & Ernzerhof, M. Generalized gradient approximation made simple. *Phys. Rev. Lett.* **77** (18), 3865–3868 (1996).
55. Murnaghan, F. D. The compressibility of media under extreme pressures. *Proceedings of the National Academy of Sciences*, 30(9), 244–247. (1944).
56. Monkhorst, H. J. & Pack, J. D. Special points for Brillouin-zone integrations. *Phys. Rev. B*. **13** (12), 5188–5192 (1976).
57. Madsen, G. K., Carrete, J. & Verstraete, M. J. BoltzTraP2, a program for interpolating band structures and calculating semi-classical transport coefficients. *Comput. Phys. Commun.* **231**, 140–145 (2018).
58. Ali, A. et al. .Exploring the magneto-optic, thermoelectric, and electronic properties of Ba_2GdXO_6 (X = Nb, & U) double perovskites by employing the DFT approach. *Chem. Pap*. **79**, 1137–1153. https://doi.org/10.1007/s11696-024-03846-z (2025).
59. Ribag, K. et al. Structural, electronic, and optical properties of vacancy-ordered double perovskite Cs2XCl6 (X = Se, Ge, and Mn) for photocatalytic applications are investigated using first-principles calculations. *Comput. Condens. Matter*. **46**, e01230. https://doi.org/10.1016/j.cocom.2026.e01230 (2026).
60. Islah, J. et al. First-principles and AIMD study of structural, magnetic, and optoelectronic properties of vacancy-ordered double perovskites Ag2BCl6 (B = Tc, Re) for advanced spintronic and optoelectronic applications. *Comput. Condens. Matter*. **44**, e01090. https://doi.org/10.1016/j.cocom.2025.e01090 (2025).
61. Ahmad Ali, B., Gul, M. S., Khan, G., Khan, A. S. & Mohamed, F. A. Unveiling the electronic, optical, thermoelectric, and magnetic properties of novel Ba2GdMO6 (M = Pa, Ta) via DFT calculation. *J. Magnetism Magn. Mater.* **604**, 172311. https://doi.org/10.1016/j.jmmm.2024.172311 (2024).
62. Salma Zahan, D. & Afroj, M. A. R. Impact of pressure on structural, mechanical, optoelectronic and thermoelectric properties of vacancy-ordered double perovskite K2SeCl6: A first principles study. *Next Mater.* **8**, 100512. https://doi.org/10.1016/j.nxmate.2025.100512 (2025).
63. Yasir, M. A., Mustafa, G. M., Adil Ameer, M., Noor, N. A. & Sohail Mumtaz, Ihab Mohamed, M. Tunability of half metallicity and thermoelectric indicators in Na2TaX6 (X = Cl, Br) vacancy ordered double perovskites. *Mater. Sci. Engineering: B* https://doi.org/10.1016/j.mseb.2024.117830 (2025).
64. Zia Ullah, B. et al. Spin-polarized electronic, optical, and transport properties of novel Cs2XMoBr6 (X = Na, Li) HDPs: First-principles study, Chem. Phys. Lett. https://doi.org/10.1016/j.cplett.2024.141471 (2024).
65. Huda, A., Alburaih, Sadia Nazir, N. A., Noor, A., Laref & Musa Saad, M. H.-E, Physical properties of vacancy-ordered double perovskites K_2TcZ_6 (Z = Cl, Br) for spintronics applications: DFT calculations, Issue 3, Issue in Progress, RSC Advances. (2024).
66. Ali, A., Anissa, B., Radouan, D., Bouzieh, N. A. & Amrane, N. Exploring the potential of lead-free double perovskites K. *(B = Cu Ag) Adv. optoelectronic thermoelectric applications: DFT study Mod. Phys. Lett. BVol*. **39**(28), 2550156 (2025).
67. Mir, S. H., Teli, N. A. & Basharat, W. Cerium-based lead-free vacancy ordered double perovskites A2CeX6(A = Cs, K and X = Cl, Br) for sustainable energy applications. *Sol. Energy*. **298**, 113705. https://doi.org/10.1016/j.solener.2025.113705 (2025).
68. Lakhdar, B. et al. Structural, electronic, elastic, optical and thermoelectric properties of ASiCl. *(A = Li Rb Cs) chloroperovskites: DFT study Opt. Quant. Electron.* **56**, 313. https://doi.org/10.1007/s11082-023-06045-4 (2024).
69. Ahmad Ali, B., Gul, M. S., Khan, G., Khan, A. S. & Mohamed, F. A. Unveiling the electronic, optical, thermoelectric, and magnetic properties of novel Ba2GdMO6 (M = Pa, Ta) via DFT calculation. *J. Magnetism Magn. Mater. Volume*. **604**, 172311. https://doi.org/10.1016/j.jmmm.2024.172311 (2024).
70. Ali, A. et al. .Exploring the magneto-optic, thermoelectric, and electronic properties of Ba_2GdXO_6 (X = Nb, & U) double perovskites by employing the DFT approach. *Chem. Pap*. **79**, 1137–1153. https://doi.org/10.1007/s11696-024-03846-z (2025).
71. , Z. U. B. et al. Spin-polarized electronic, optical, and transport properties of novel Cs2XMoBr6 (X = Na, Li) HDPs: First-principles study. *Chem. Phys. Lett.* **850**, 141471. https://doi.org/10.1016/j.cplett.2024.141471 (2024).
72. Snyder, G. J. & Toberer, E. S. Complex thermoelectric materials. *Nat. MaterialsVOL* **7**, 105 (2008).
73. Nipa, N. A., Afridi, A. M. & Mohammad, A. R. Band gap and optical property modulation under pressure in vacancy-ordered double perovskite Cs2SeCl6, Comput. Theoret. Chem., **1235**, 114572. https://doi.org/10.1016/j.comptc.2024.114572 (2024).
74. Ameur, R. et al. Half-metallicity and spin-gapless semiconducting properties in FeCrTiM (M = Al, As, Si) quaternary heusler alloys for spintronic, thermoelectric and optoelectronic applications. *Adv. Compos. Hybrid. Mater.* **8**, 366. https://doi.org/10.1007/s42114-025-01466-z (2025).
75. Djelti Radouan, B., Lakhdar, B., Anissa, A. & Ali Bendehiba S. A. Multifunctional properties of cubic vacancy-ordered double halide perovskites A2BBr6 (A = Rb, Cs; BS, se) for optoelectronic and thermoelectric applications. *Mater. Chem. Phys.* **353**, 132114. https://doi.org/10.1016/j.matchemphys.2026.132114 (2026).

Acknowledgements

The authors are thankful to the Deanship of Graduate Studies and Scientific Research at Najran University for funding this work under the Elite Funding Program grant code (NU/EP/SERC/14/4228-1).

Author contributions

Conceptualization: Elkenany Brens ElkenanData curation: Murat Yaylacı Formal analysis: Hasan B. Albargi,

Aseel Smerat, Ramzi Dhahri, A. M. AbdelghanyValidation: M. Fatmi.

Declarations

Competing interests

The authors declared no potential conflicts of interest with respect to the research, authorship, and/or publication of this article.

Additional information

Correspondence and requests for materials should be addressed to E.B.E.

Reprints and permissions information is available at www.nature.com/reprints.

Publisher's note Springer Nature remains neutral with regard to jurisdictional claims in published maps and institutional affiliations.